Purdue University
Purdue e-Pubs

Open Access Theses | Theses and Dissertations

12-2016

Helical strakes on High Mast Lighting Towers and their effect on vortex shedding lock-in

Ayah Zahour
Purdue University

Follow this and additional works at: https://docs.lib.purdue.edu/open_access_theses

 Part of the Aerospace Engineering Commons

Recommended Citation
Zahour, Ayah, "Helical strakes on High Mast Lighting Towers and their effect on vortex shedding lock-in" (2016). *Open Access Theses*. 912.
https://docs.lib.purdue.edu/open_access_theses/912

This document has been made available through Purdue e-Pubs, a service of the Purdue University Libraries. Please contact epubs@purdue.edu for additional information.

Graduate School Form
30 Updated 12/26/2015

PURDUE UNIVERSITY
GRADUATE SCHOOL
Thesis/Dissertation Acceptance

This is to certify that the thesis/dissertation prepared

By Ayah Zahour

Entitled
HELICAL STRAKES ON HIGH MAST LIGHTING TOWERS AND THEIR EFFECT ON VORTEX SHEDDING LOCK-IN

For the degree of Master of Science in Aeronautics and Astronautics

Is approved by the final examining committee:

Steven H. Collicott
Chair

John P. Sullivan

Robert J. Connor

To the best of my knowledge and as understood by the student in the Thesis/Dissertation Agreement, Publication Delay, and Certification Disclaimer (Graduate School Form 32), this thesis/dissertation adheres to the provisions of Purdue University's "Policy of Integrity in Research" and the use of copyright material.

Approved by Major Professor(s): Steven H. Collicott

Approved by: Weinong Wayne Chen 12/1/2016

Head of the Departmental Graduate Program Date

HELICAL STRAKES ON HIGH MAST LIGHTING TOWERS AND THEIR EFFECT ON VORTEX SHEDDING LOCK-IN

A Thesis

Submitted to the Faculty

of

Purdue University

by

Ayah Zahour

In Partial Fulfillment of the

Requirements for the Degree

of

Master of Science in Aeronautics and Astronautics

December 2016

Purdue University

West Lafayette, Indiana

To my family

ACKNOWLEDGEMENTS

First and foremost, I would like to thank my advisor, Dr. Steven Collicott, for his guidance, patience, and mentorship whom without this life learning experience would not have been possible. Thank you for the great opportunity in learning from you and for working under your supervision.

A great thank you to my family, especially my mother, sister, stepfather, and grandfather for their proud and undying support. A special dedication to my late father, Dr. Zahour, for the inspiration that his achievements have provided me.

A thank you to Dr. Sullivan and John Phillips for their great help and assistance during the setup of this project. Thanks to Dr. Sullivan and Dr. Connor for being part of the thesis committee.

Finally, a thank you to my many supportive friends for their help, insight, and encouragement throughout this process.

TABLE OF CONTENTS

LIST OF TABLES

LIST OF FIGURES

LIST OF SYMBOLS

Re	Reynolds Number
f_s	Shedding Frequency
U_∞	Free Stream Velocity
D	Diameter
St	Strouhal Number
ν	Kinematic Viscosity
μ	Dynamic Viscosity
P_s	Static Pressure
P_t	Total Pressure
ρ	Density
τ	Shear Stress
S_c	Scruton Number
m	Mass per Unit Length
m^*	Mass Ratio
δ	Logarithmic Decrement
ζ	Damping Ratio

LIST OF ABBREVIATIONS

FFT	Fast Fourier Transform
VIV	Vortex Induced Vibration
TLD	Tuned Liquid Damper
TIAT	Tokyo International Airport Tower

ABSTRACT

Zahour, Ayah. M.S.A.A., Purdue University, December 2016. Helical Strakes on High Mast Lighting Towers and their Effect on Vortex Shedding Lock-In. Major Professor: Dr. Steven H. Collicott.

An experimental study on the effect of helical strakes on vortex induced vibrations and the lock-in phenomenon in High Mast Lighting Towers (HMLTs) is investigated. Two multi-sided tapered scaled models are clamped in place in a subsonic wind tunnel that is equipped with a hot-wire sensor and a traverse mechanism. The shedding frequency data is collected for the models with and without helically patterned strakes with the use of two different ropes. The responses of the tower models, for a Reynolds number of 44, 000, are compared and discussed under different configurations including: two directions of the model with respect to the direction of the flow, and changes in the ratio of strake height to HMLT diameter. Four major aspects of the spectrum of the hot-wire signal from the wake are studied: the vortex shedding frequency, signal strength, characteristic spectral peak area, and characteristic spectral peak width. It is observed that, for most cases, no specific method produces a decisive outcome. However, some of the results for the 12-sided model provide supporting evidence that the vortex induced vibrations may be mitigated with the use of helical strakes.

CHAPTER 1. INTRODUCTION

1.1 Background

High Mast Lighting Towers (HMLTs) are widely used countrywide in areas that need widespread illumination such as national highways, local highways, major interchanges, and intersections. Standard HMLTs are typically 100 ft. to 160 ft. high with a base diameter between 2 ft. and 2.5 ft. and a tip diameter of 8 inches to 12 inches. They are tapered multi-sided structures, generally 12- or 16-sided, typically with a taper ratio of 0.14 inches per foot [1, 2]. In addition to their light and elastic nature, these HMLTs are equipped with a form of light fixtures called luminaires and a lowering device used for servicing the luminaires [3]. Both features create an additional concentrated mass on a slender and flexible pole, a structure already predisposed to fatigue loading.

1.2 Purpose of the study

Because of their slender structure and low structural damping values, HMLTs and highly susceptible to aeroelastic effects, mainly vortex shedding vibrations and a phenomenon known as “Lock-in”. HMLTs experience oscillations from natural wind gusts that lead to increased fatigue, unpredictable fatigue loads, and at times failure and collapse of the structure. “Lock-in”, further explained in the Theory section, is an unwanted phenomenal result of vortex-induced vibrations. In a Ph.D. dissertation research study, Ocampo studied the phenomena of lock-in and described it as span-wise regions of a

tapered HMLT that, due to wind effects, shed vortices at the same frequency despite the differing diameters throughout those regions. The ensuing results can be catastrophic if these frequencies happen to be near the natural frequency of the structure or one of its modes for sufficiently long times [2]. Due to wind-induced excitations, some of these HMLT structures have experienced high fatigue loading and failed less than five years into service [1]. After a mere two years of service, a high mast lighting pole near Sioux City in Iowa collapsed in 2003. A post-collapse picture of the pole is shown in Figure 1.1 (a). An investigation of the collapse revealed that the failure was attributed to vortex induced vibrations and loadings [4]. During a winter storm that affected Western Illinois in 2003, an alarming number of 140 highway light poles failed due to a large-amplitude excitation of the structures [5]. One such collapsed poles is shown in Figure 1.1 (b). A large number of the structures that have collapsed have had fatigue failure observed at the bottom part of the pole, more specifically at the baseplate-to-column weld area. Other observed failure locations have been at the anchor rods or at the handhole details [1]. A baseplate fatigue damage example can be seen in Figure 1.1 (c).

(a) (b) (c)

Figure 1.1 Fatigue damage and collapses: (a) HMLT collapse near Sioux City, IA (2003) [4], (b) Tower collapse near Galesburg, IL (2003) [5], (c) Fatigue damage of baseplate joints [6]

Various devices have been implemented in the industry to attempt to suppress the magnitude and effect of vortex induced vibrations. One such method is the use of helical strakes to mitigate vortex shedding and prevent lock-in from occurring. A team of civil engineers at Purdue University has conducted a full-scale in-field study of 3 HMLTs retrofitted with helical strakes. One of the configured HMLTs is shown in Figure 1.3. The study consisted of a 2-phase experiment. First, two different configurations were used for the HMLTs with either single- or double-strake retrofits, shown in Figure 1.2, and their responses were monitored over a set period of time. The second phase of the experiment consisted of examining the response of the full scale HMLT with a double helical strake installed either across the full length of the pole or at only the top tier of the pole. The engineers found that all the strake disruption configurations were in fact successful in reducing the effect of vortex shedding induced excitations. However, the effectiveness of each method differed. The one proven most effective method at suppressing vortex

induced vibrations and reducing the fatigue loading, was the double-strake configuration installed across the length of the model.

This thesis research study was motivated by the potential in the use of helical strakes in HMLTs as a low-cost, easy to install, vortex induced vibrations suppression method.

In this thesis, a subsonic wind tunnel setting study was performed on two scaled 12- and 16-sided tapered HMLT models that are fitted with two different diameter ropes in a helical pattern. This configuration is a type of “spiral” disruption to the models oscillation shear layer behavior, and hence its aerodynamic properties, with the purpose of controlling the induced vortex vibrations by means of manipulating its response to structural excitation.

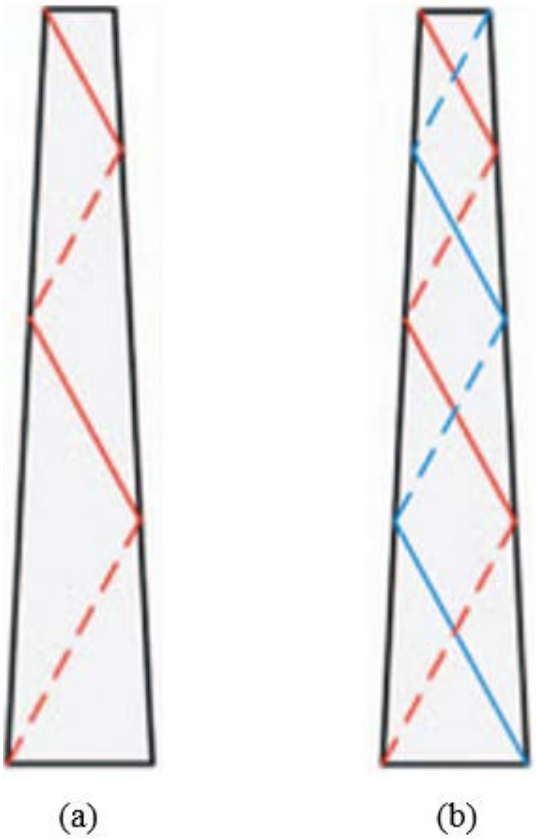

Figure 1.2 Strake configurations: (a) single, (b) double

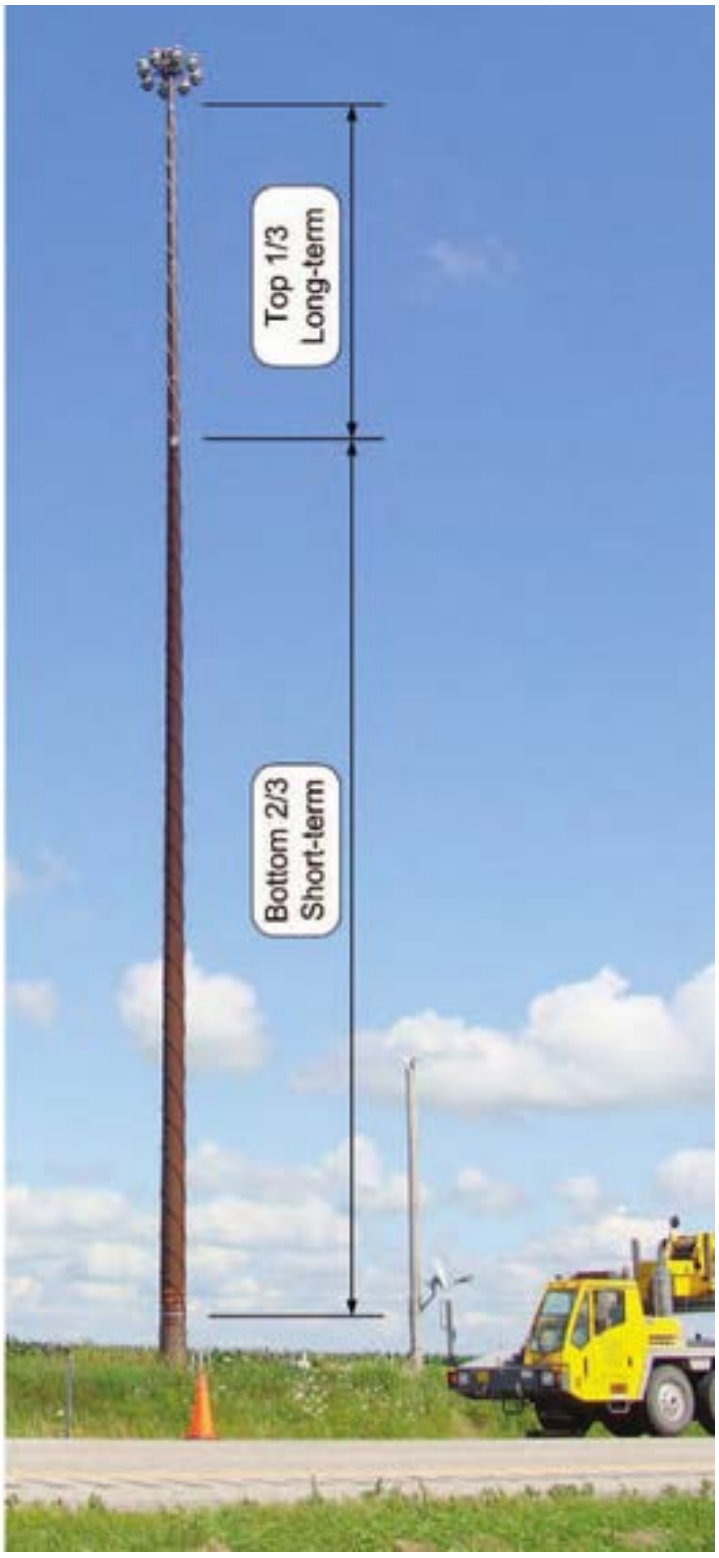

Figure 1.3 High Mast Lighting Towers with helical strakes

1.3 Content Summary

This thesis is divided into six chapters. Chapter 2 discusses the theory behind vortex induced vibrations and the lock-in phenomenon. A literature review associated with wind-induced vibration suppression methods is presented in Chapter 3. Chapter 4 describes the setup and procedures followed during the experiment and the data processing methods. A thorough analysis of the experimental results is discussed in Chapter 5. Finally, Chapter 6 summarizes the prominent findings of the study and provides recommendations for future possible work.

CHAPTER 2. THEORY

This section describes the process by which the “Lock-In” phenomena occurs. First, the boundary layer theory is explained followed by a description of the flow around a circular cylinder at different Reynolds numbers. The flow separation over a cylinder, vortex shedding and the resulting vortex induced vibrations are explained in this section. All elements are finally tied together to describe “Lock-in” and the dangerously resulting fatigue failure of bluff bodies such as High Mast Lighting Towers.

2.1 Boundary Layer Theory

Shear stress τ exists everywhere in a flow given a velocity gradient across streamlines. Friction plays an important role in regions where velocity gradients are substantial. The flow field far from the surface of a body is usually considered inviscid while a thin region where the flow is adjacent to the surface is treated as viscous. This natural separation of the flow results in two distinct regions where the layer close to the surface of the body greatly affected by friction is called the “Boundary Layer” [7]. A thin layer of air molecules sticks to the surface of a body and has a velocity of zero relative to the surface. This condition is called the “no-slip” condition and is responsible for the large velocity gradients within the boundary layer.

From the surface, the flow velocity rises rapidly to the velocity outside the boundary layer within a small distance, δ, as shown in Figure 2.1. The boundary layer thickness is defined as the thickness where the velocity reaches 99% of the local free stream velocity. The boundary layer grows larger as it moves downstream as shown in the development of a boundary layer along a flat plate example in Figure 2.2. The slope of the velocity profile at the wall, $(dU / dy)_{y=0}$, defined as the velocity gradient at the wall governs the wall shear stress τ_w as described by (2.1), where μ is the viscosity.

$$\boldsymbol{\tau_w = \mu\left(\frac{dU}{dy}\right)_{y=0}} \tag{2.1}$$

The velocity profiles through a boundary layer are different depending on the nature of the flow. As shown in Figure 2.3, the turbulent boundary layer profile is fuller than the laminar profile and the velocity is close to the free stream velocity but rapidly decreases to zero near the surface. On the other hand, the laminar profile is steeper but the velocity gradually decreases to zero from the outer edge to the surface [7].

It is clear from Figure 2.3 that the velocity gradient at the wall, $(dU / dy)_{y=0}$, for a turbulent flow is larger than that of a laminar flow. Using equation (2.1) and assuming that μ is constant, it is demonstrated that the turbulent shear stress is higher than the laminar shear stress, $(\tau_w)_{Turbulent} > (\tau_w)_{Laminar}$.

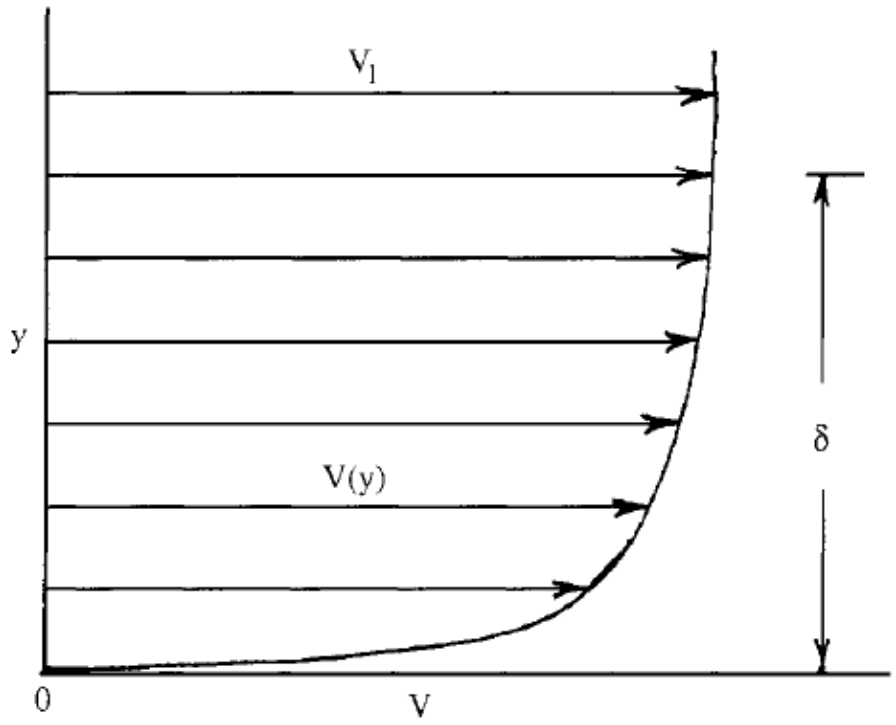

Figure 2.1 Typical Boundary Layer [8]

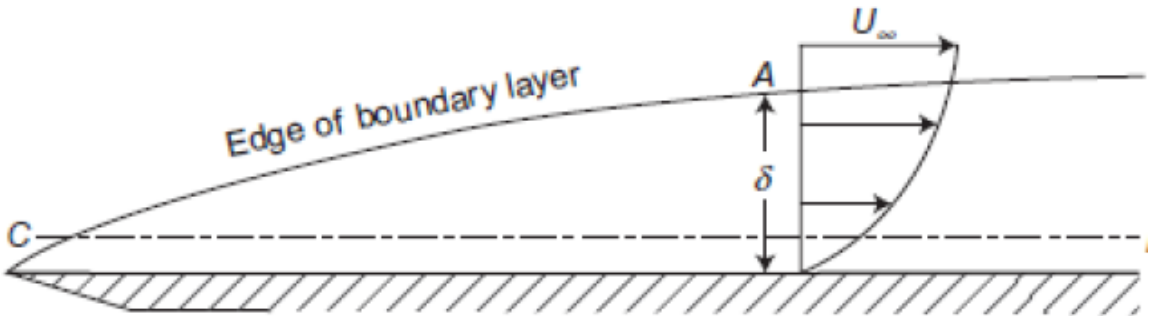

Figure 2.2 Boundary Layer Development along a Flat Plate [9]

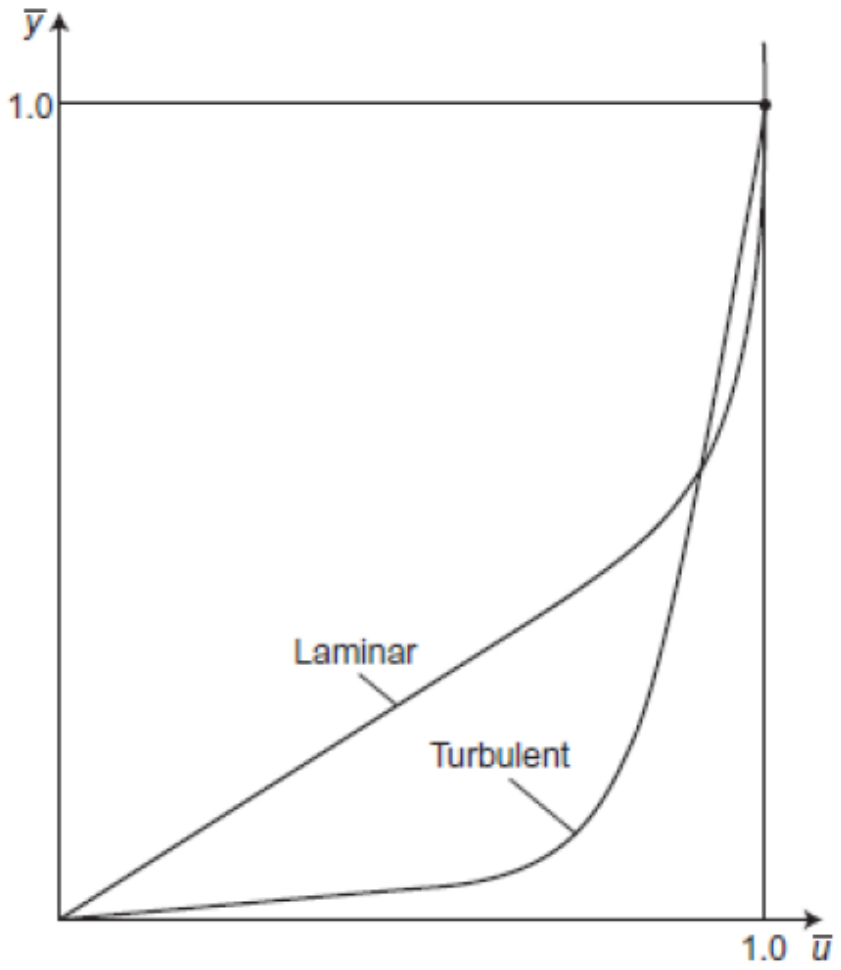

Figure 2.3 Comparison between Laminar and Turbulent Boundary Layer [9]

2.2 Flow over a cylinder

Often, when a body is travelling through a fluid such as water or air, the flow over its surface is smooth and remains attached to the surface of the body. However, the flow over a surface and the patterns that develop behind the body are far more complicated and are affected by different variables.

The wake describes the flow pattern behind a bluff body when a fluid passes the body, the behavior of which is directly related to the velocity of the fluid. The flow past a circular cylinder, a bluff body, has been widely studied and described extensively in many articles and textbooks. The wake behind a circular cylinder, shown in Figure 2.4, exhibits different flow patterns according to the flow velocity and hence the cylinder's Reynolds number, Re, defined by Equation (2.2):

$$\boldsymbol{Re} = \frac{\boldsymbol{U_\infty D}}{\boldsymbol{\nu}} \tag{2.2}$$

where U_∞ is the free stream velocity, D is the diameter of the cylinder, and ν is the kinematic viscosity. The Reynolds number can also be described as the ratio of the inertial effects to viscous effects.

At very low Reynolds numbers, less than 4, there is no wake as the flow over a circular cylinder is attached to the body and the streamlines are smooth and nearly symmetrical as seen in Figure 2.4(a). As the Reynolds number increases from 4 to approximately 40, separation occurs and a wake is formed behind the cylinder. A deficit between the free stream velocity and the velocity in the wake can be successfully related to the drag force acting upon the cylinder. In Figure 2.4(b), two separate and stationary vortices form behind the cylinder, called Foppl vortices. Once the Reynolds number reaches a value of

about 35 to 40, vortices start to alternate and are shed periodically behind the cylinder from each side due to flow instability. This vortex shedding phenomena is famously known as the Von Karman Vortex Street, shown in Figure 2.4(c). This oscillating flow behind the body is particularly of interest in this thesis and further detailed in relation to vortex-induced vibrations in Section 2.4. When the Reynolds number reaches values on the order of 10^5, the vortex street experiences turbulence. Because of the adverse pressure gradient (a pressure rise in the flow along its same direction), fluid mass within the boundary layer experiences retardation. To overcome the adverse pressure gradient, fluid mass needs energy. However, due to the friction forces between the flow and the body surface, part of the energy is lost and the fluid comes to rest before reaching the rear stagnation point. The boundary layer then separates from the surface of the cylinder as seen in Figure 2.4(d). Figure 2.4(e) shows the flow pattern behind a cylinder for a Reynolds number between 3×10^5 and 3×10^6, where the flow transitions to turbulence and the wake becomes narrower and more disorganized.

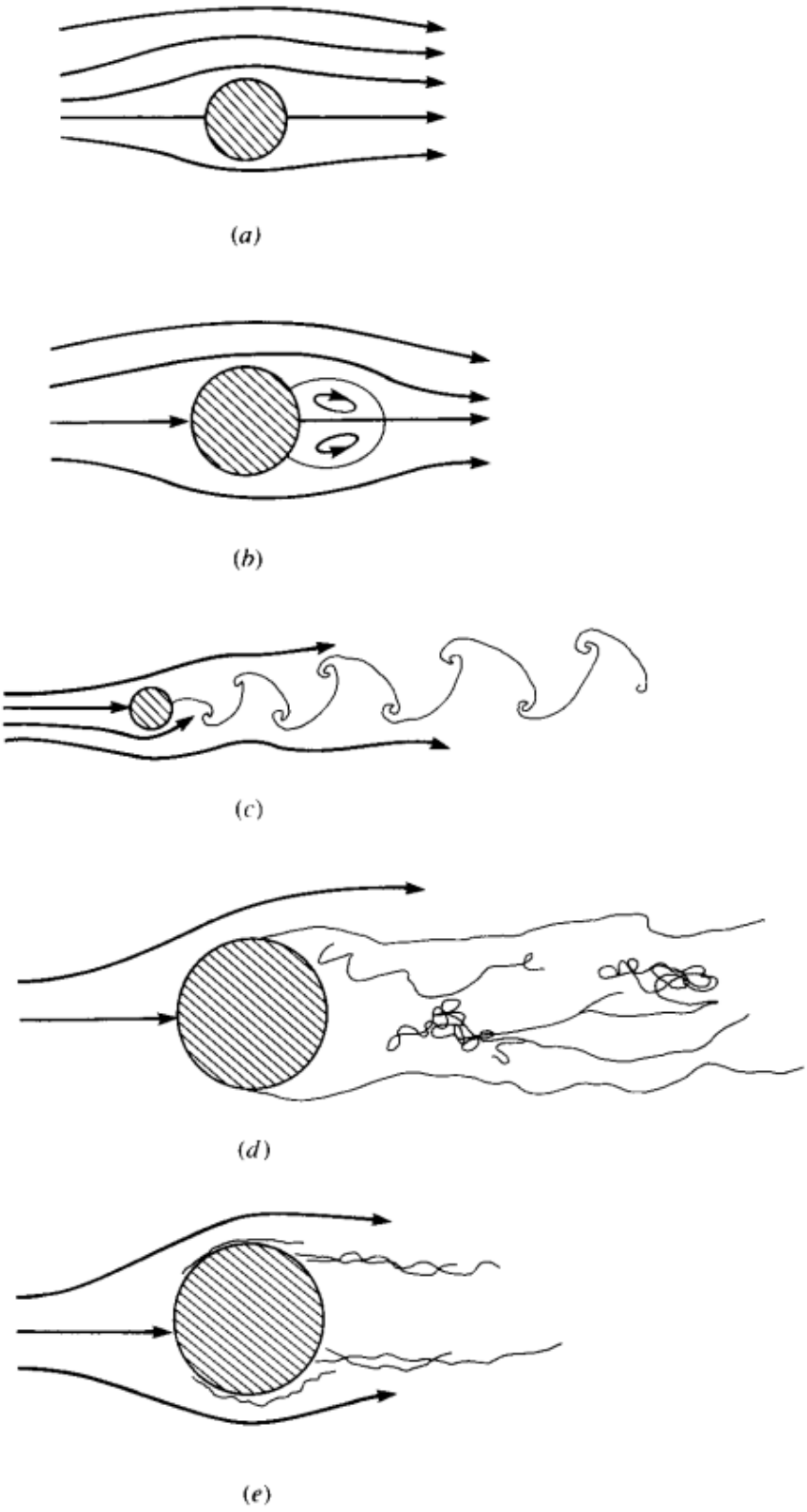

Figure 2.4 Flows Patterns over a Circular Cylinder [7]

2.3 Vortex Shedding

When the Reynolds number of a flow past a blunt body is increased to a critical value, an oscillating flow takes place behind the body. Due to the unsteady separation of the flow over the body, low-pressure zones (vortices) are generated and detach periodically from each side of the cylinder. The alternating shedding zones from the top and bottom sides of the body form rows of vortices and create an organized pattern in the wake known as the Von Karman Vortex Street. Figure 2.5 is a good visual example of the Von Karman Street made visible by water electrolytic precipitation [10]. Each vortex in this phenomenon is distinctively located midway between two vortices on the opposite-side vortex row. Vortex shedding is a complex phenomenon that can occur in both laminar and turbulent flow but is highly dependent on the flow velocity as well as the shape and size of the body among other variables.

The vortices shed at a particular frequency, which is defined by the non-dimensional Strouhal number described by the following equation:

$$\boldsymbol{St} = \frac{\boldsymbol{f_s D}}{\boldsymbol{U_\infty}} \tag{2.3}$$

where f_s is the vortex shedding frequency, D is the diameter of the cylinder and U_∞ is the free stream velocity of the flow.

Many studies have been conducted to collect experimental data regarding the flow over a cylinder. Much of this data has been collected to create the plot shown in Figure 2.6. The envelope in the figure is defined by a collection of data from studies performed by different scientists and is considered to be “the best estimate of the Strouhal-Reynolds relationship for eddies on rigid cylinders that can be made at this time” [11]. Although

the scientific bulletin written by Lienhard was published in 1966, the Strouhal-Reynolds relationship chart is widely used and considered to be reliable to this day.

From Figure 2.6, a near-constant Strouhal number of 0.21 can be observed for a Reynolds number range of $10^4 < Re < 10^6$. This Reynolds number is of interest in this study as it is the range that HMLTs experience in the field.

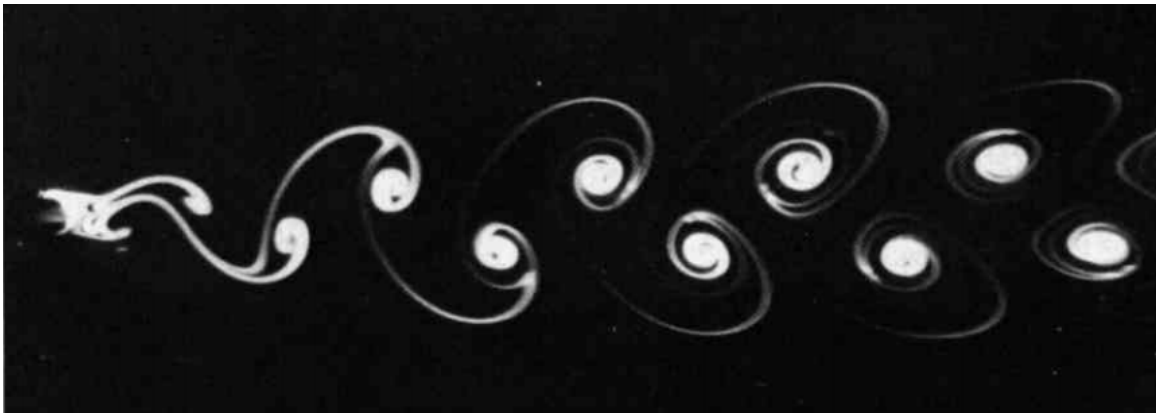

Figure 2.5 Von Karman Street behind a cylinder at Re = 105 [10]

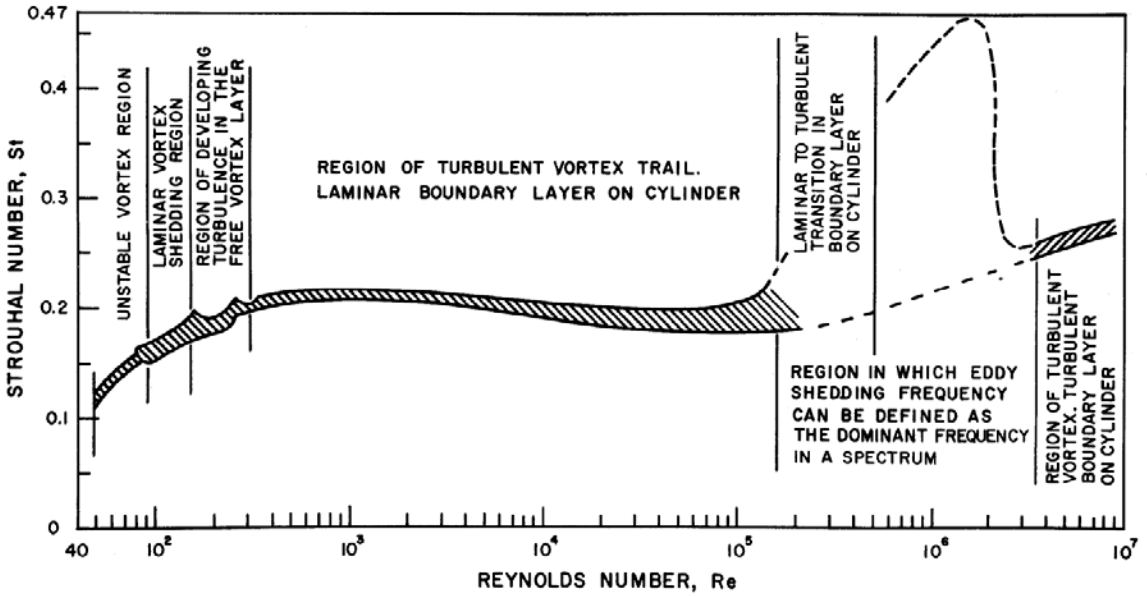

Figure 2.6 Strouhal Number vs. Reynolds Number Relation [11]

2.4 Vortex Induced Vibrations (VIV)

For the special case of a cylinder and at a Reynolds number of approximately 40, eddies around the body starts shedding periodically – at a calculable frequency – from alternate sides of the cylinder. These vortices from the Von Karman Street generate low pressure zones, or pockets, on alternate sides of the body and produce a periodic irregularity in the flow pattern around the bluff body.

The fluid under which the body is subjected moves to fill the voids created by the vortices that result in an uneven pressure distribution on the surfaces of the body. Vortices then generate a lateral load or aerodynamic lift forces leading to structural vibrations.

In summary, structural vibrations are induced on the cylinder due to the oscillatory forces caused by the vortex shedding, a phenomenon known as Vortex Induced Vibrations (VIV).

Slender and uniform bodies typically experience vortex induced vibrations that can lead to structural fatigue and ultimately failure. Many structures are exposed to vortex induced vibrations including but not limited to towers, masts, bridges, cables, stacks and even car antennas. In particular, free standing slender structures such as High Mast Lighting Towers are particularly susceptible to vibrations and are constantly exposed to winds. If a structure is already experiencing structural fatigue, including cracks at the base for HMLTs, a strong gust of wind can be fatal. For this reason, it is important for engineers to carefully design such structures as to effectively avoid fatigue failures caused by structural vibrations.

2.5 Lock-in

Due to the vibrations induced by vortex shedding, a pole can experience large amplitude structural oscillations. The second mode vibration of a structure, or “Resonance”, is due to the transverse oscillating forces driven by the alternating vortex shedding.

If the vortex shedding frequency coincides with the natural frequency of the body or one of its modes, a condition known as “Lock-in” occurs. The “Lock-in” condition can still occur over a range of velocities, thus independently from the Strouhal number as shown in Figure 2.7. Report 718 of the National Cooperative Highway Research Program states that “Locking-in to a range of velocities means that small fluctuations in wind speed or pole diameter do not alter the frequency of the vortex shedding and therefore results in continued resonance” [1]. The persisting resonance of the pole causes load-induced fatigue and can lead to structural failure. Such failure happens generally at the base of the structure and results in the collapse of the pole. A picture of an antenna tower collapse from fatigue failure presented by Giosan et al. is shown in Figure 2.8.

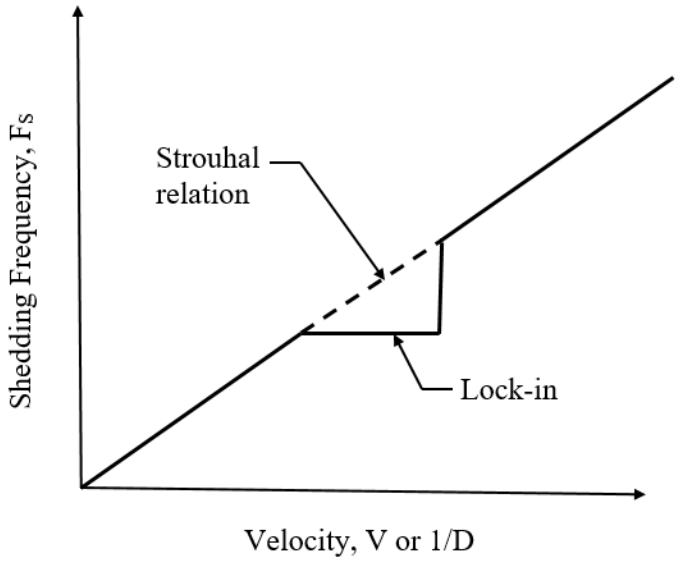

Figure 2.7 Lock-in phenomenon

Figure 2.8 Antenna Tower Collapse [12]

Interestingly, lock-in can also happen for tapered poles as mentioned by Ocampo for his PhD dissertation. Ocampo states that taper affects the vortex shedding of poles by the creation of “vortex cells”, an aerodynamic phenomenon defined as “an axial region with coherent shedding with the same frequency for a range of different diameters on a tapered structure” [2].

Figure 2.9 is a model representation of the effect of taper on vortex shedding and the subsequent vortex cells. The lines represent the center of a vortex and the frequency at which it sheds. From the Strouhal relation, defined by Equation (2.3), we should expect a proportional inverse relation between the diameter of the pole and the shedding frequency. However, vortex cells result in “a section of the pole [that] may lock in exclusively to the fundamental frequency or more than one structural modal frequency” [2].

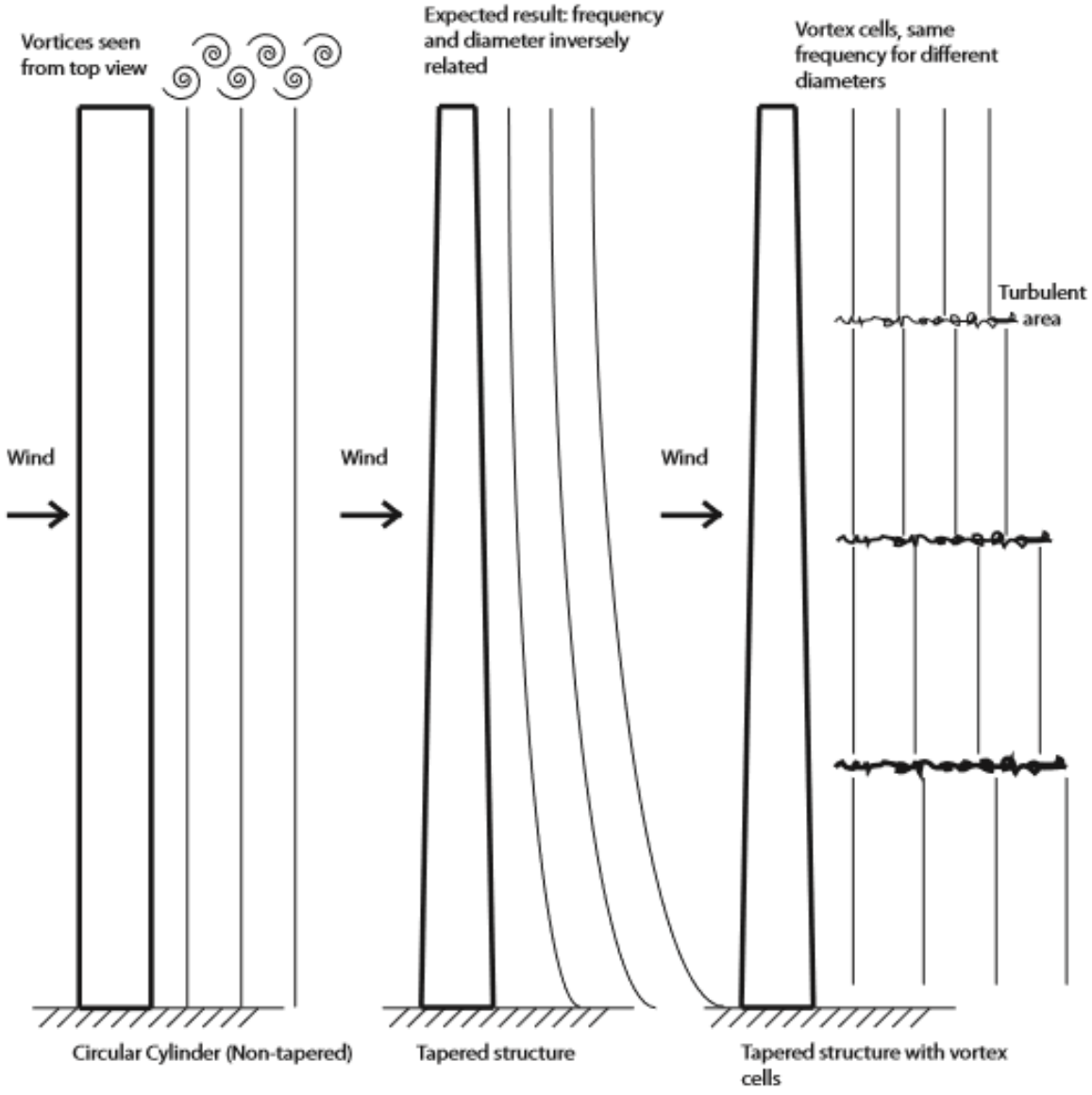

Figure 2.9 Vortex Shedding on Non-Tapered and Tapered Poles [2]

CHAPTER 3. LITERATURE REVIEW

There are different types of structural flow induced vibrations including galloping, flutter, buffeting, and vortex induced vibrations. Each phenomenon is a specific complex excitation response to the fluid flow and is dependent on the flow nature, flow velocity and direction, structure stiffness, and even weather conditions amongst other variables. Galloping is a one dimensional “self-excited phenomenon characterized by low frequency, large amplitude vibrations” [13]. Exhibiting similar behavior, flutter is also a self-feeding phenomenon but is categorized with a coupled oscillation modes [13]. One famous example of failure caused by flutter is the collapse of the Tacoma Narrows bridge in 1940 where both vertical and torsional vibrations led to the collapse of the bridge [14]. In the report of the “Failure of the Tacoma Narrows Bridge”, a study written in response to the failure of the bridge, Von Karman et al. stated that aggravated torsional oscillations of the bridge in addition to large amplitude oscillations caused by natural winds caused the ultimate failure and collapse of the structure [14]. On the other hand, buffeting is a non-self-induced excitation mainly caused by velocity fluctuations and flow turbulence from natural wind gusts [3].

Vortex shedding induced vibrations is a phenomenon that, under certain conditions, can lead to lock-in which occurs at specific ranges of fluid velocities as explained in the previous section. Unlike vortex shedding induced vibrations, the amplitude of vibrations

for all the other three phenomena (galloping, flutter, and buffeting) increases as the flow velocity increases.

Due to their slender structure and low structural damping values, high mast lighting towers are highly vulnerable to aeroelastic effects manifested through vortex induced vibrations and buffeting which can lead to fatigue damage and potentially failure or collapse of the structure. From a practical standpoint, it is important to have a basic understanding of the phenomena described earlier; however, the main focus of this study is related to vortex induced vibrations, lock-in mechanism in high mast lighting towers, and the means to suppress said vibrations.

Vortex induced vibrations are experienced daily by a wide range of structures including but not limited to marine risers, cables, towers, chimneys and buildings. Many studies have been performed to reduce or suppress vortex induced vibrations in these structures. The different methods commonly used to control these vibrations are characterized as either “Structural” or “Aerodynamic and Hydrodynamic” and discussed in the following two sub-sections.

3.1 Structural Methods

Structural methods can be used either by increasing the structural damping or by increasing the natural frequency of the structure to avoid resonance and hence the lock-in phenomenon.

Controlling the structural damping can be achieved by manipulating the variables within the mass-damping parameter for flexible structures known as the Scruton number [15]:

$$S_c = \frac{2m\delta}{\rho D^2} = \pi^2 m^* \zeta \tag{3.1}$$

Increasing the reduced damping could be achieved by either increasing the mass ratio, m^*, or by increasing the damping ratio, ζ, also defined as $\zeta = \frac{\delta}{2\pi}$. On the left hand side of the Scruton number relation, m is the mass per unit length, δ is the logarithmic decrement, ρ is the fluid density, and D is the cross-section diameter of the structure [15]. One way of increasing damping is by utilizing a Tuned Liquid Damper (TLD), which is a liquid-filled container that is generally placed at the top tier of buildings or towers. Through the sloshing motion within the liquid dampers, the energy is used to reduce the dynamic excitation experienced by buildings under strong winds [13]. A study performed in Japan titled "Effectiveness of tuned liquid dampers under wind excitation" successfully demonstrates the efficacy of the liquid dampers in full-scale tall buildings and towers. Wind-induced responses were monitored and measured for the Tokyo International Airport Tower (TIAT) during a period of 13 months. The first 6 months of the trial were recorded for the tower without any dampers while the following 7 months were for the tower with tuned liquid dampers installed from the floor up to the ceiling in a room located near the top of the building [16]. As seen in Figure 3.1, the damping ratio, ζ, significantly increased from 0.77% to 3.9% thanks to the tuned liquid damper. The damping ratio hike successfully increases the reduced damping described by (3.1). Another full-scale experiment was conducted by Caracoglia et al. in a laboratory setting at the University of Illinois at Urbana-Champaign, where an impact damper was attached to a 13.7 meter tapered aluminum luminaire. The installation of the chain damper, optimized for the first mode, was considered a cheap and effective passive control device [5]. It can be clearly seen from Figure 3.2, that the excitation amplitude response of the pole considerably decreased with the chain damper after only a few cycles [5].

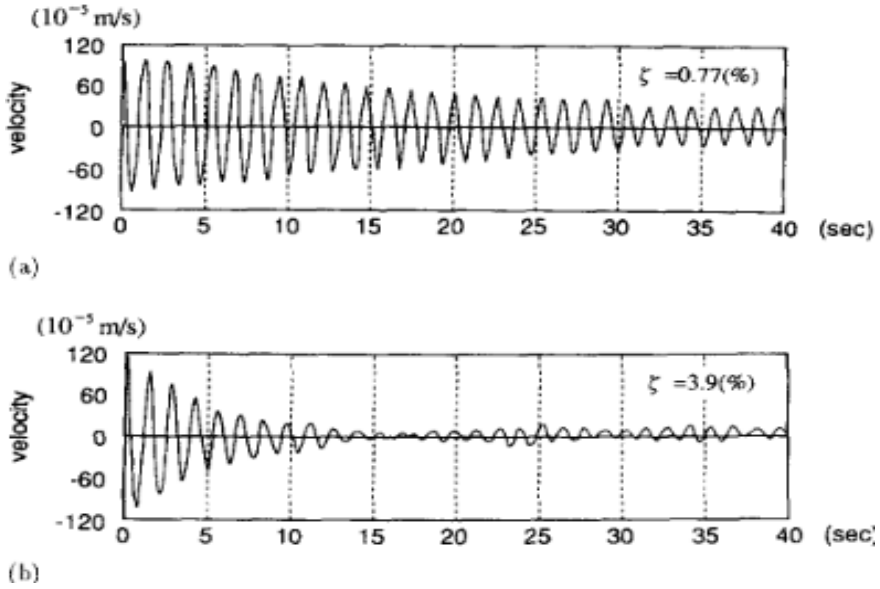

Figure 3.1 TIAT damped-free oscillations (a) without TLD, (b) with TLD [16]

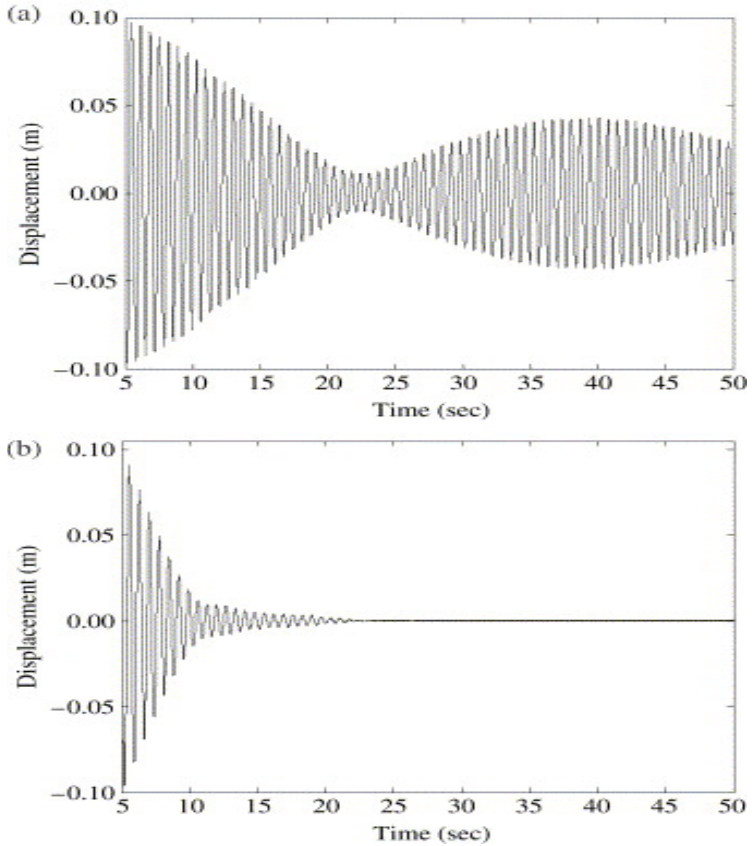

Figure 3.2 Displacement of tapered pole (a) without damper, (b) with damper [5]

A different structural method is the manipulation of the natural frequency of a structure in order to avoid resonance [13]. For the special case of lock-in, the frequency of the induced vibrations due to vortex shedding coincides with the natural frequency of the structure or one of its modes. If this condition occurs, the resulting fatigue of the structure can rapidly lead to failure and collapse. Increasing the natural frequency of a structure can be attained by the mass redistribution or the stiffening of said structure [17]. However, this method can be proven to be costly and impractical if poles have already been constructed and/or installed in the field.

3.2 Aerodynamic and Hydrodynamic Methods

There are different preventative and effective methods currently in use for all types of tubular slender structures in different areas of engineering including wind and marine applications.

A thorough review performed by Zdravkovich classifies different types of aerodynamic and hydrodynamic means to prevent vortex shedding which is the main source of induced oscillations on cylinders. “Review and classification of various aerodynamic and hydrodynamic means for suppressing vortex shedding” discusses two theories, namely an “entrainment layer” and a “confluence point” that are linked to the formation of vortex shedding and different ways to prevent their occurrence [17]. Zdravkovich states that the “entrainment layers” provide stationary fluid that feed the vortices during the vortex shedding mechanism within the wake in the separated flow region, while the “confluence point marks the region where the two entrainment layers coming from the opposite sides of the cylinder meet and interact” [17]. If a mechanism can perturb the entrainment layer, separated shear layer or the confluence point, then the oscillatory behavior exhibited

through vortex shedding and lock-in can be successfully controlled. The literature review has revealed that the aerodynamic and hydrodynamic methods can be classified into three major categories: geometric streamlining, surface modifications, and add-on devices. All categories are reviewed in the next following sub-sections.

3.2.1 Geometric Streamlining

One popular vortex induced vibration mitigation method in the marine engineering field is the implementation of streamlining, or the reduction of the bluffness of the body. In a study of passive mechanisms to control vortex induced vibrations, Kumar et al. discuss streamlining methods to weaken vortex shedding and decrease drag in liquid flow and marine uses such as marine risers, oil rigs, and piers. The use of this category of devices can affect the switch of the confluence point and delay the occurrence of vortex shedding downstream of the flow [17]. Two such methods, streamline fairings and guide vanes, are presented in Figure 3.3. The streamline fairings are commonly used in deep water marine settings and have been proven to reduce vortex induced vibrations by up to 80% while also reducing drag [13]. These airfoils shaped fairings can liberally rotate around the body to which they are attached to and alter their direction to align with the fluid flow [13]. Guide vanes, shown in Figure 3.3 (b), are very similar to fairings but are characterized by a distinct and sharp trailing edge. Although successful in suppressing vortex shedding induced vibrations, streamlining mechanisms are expensive to manufacture, difficult to install due their size and the environment in which they operate, and are prone to fast biological marine growth accumulation on the surfaces.

3.2.2 Surface Modifications

Another method proven to successfully reduce vortex induced vibrations are surface modifications. These modifications can be manifested through the addition of smooth curved protrusions applied directly to the surface of an elongated body as shown in Figure 3.4 [18]. The example shown in the figure is from a US patented invention created by Bearman et al. in 2005. The elliptically shaped protuberances are radially arranged along the cylinder in pairs within a range of 30 degrees to 45 degrees between each set of protrusions to account for a variance in the flow direction [18]. The example protuberances, shown in Figure 3.4, have a height of half the diameter of the cylinder and are spaced 1.75 diameters along the cylinder. They are able to reduce drag by 24%, subsequently reducing the structural vibrations due to vortex shedding [18]. Such modifications are commonly used for chimneys, wind turbines, offshore platforms and marine risers [13].

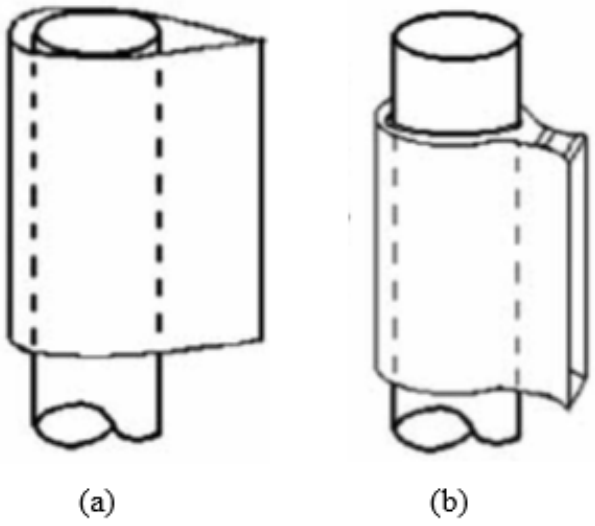

Figure 3.3 Structural geometry streamlining: (a) streamline fairing, (b) guide vane [13]

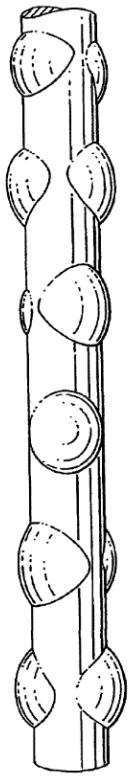

Figure 3.4 Smoothly curved protuberances [18]

3.2.3 Add-on Devices

An extensive array of add-on devices to control vortex induced vibrations have been studied and tested. However, different mechanisms have been successful in curbing vortex induced vibrations and the resulting lock-in phenomenon in some cases but have been unsuccessful in other scenarios. Most research pertaining to add-on devices has been restricted to cylinders only, but many solutions can be directly applied to slender tubular multi-sided structures and more specifically high mast lighting towers. The following discussion describes some of these devices and their success rate in controlling vortex induced vibrations.

Add-on devices can be divided into two main categories: surface protrusions (Figure 3.5) and shrouds (Figure 3.8).

Surface protrusions are devices, made generally from wires, strakes, fins, or spheres, that are retrofitted around the structure that is experiencing oscillations due to natural wind gusts or strong currents. These devices alter the shape of a structure and are successful when they are able to distress the separated shear layers and separation lines by promoting an artificial turbulence within the boundary layer of the cylinder, encouraging a premature transition to turbulence [17].

In his review, Zdravkovich presented a broad list of surface protrusions, shown in Figure 3.5, classified as either omnidirectional means or unidirectional means. Omnidirectional means are defined as ones that "are not affected by the direction of fluid velocity", while unidirectional means are "effective only in one direction of velocity" [17]. A "+" sign next to the design represents a successful vortex induced vibrations suppression mean, while a "-" sign represents an ineffective method, or even an adverse mean contributing to a growth in oscillations amplitude [17]. Table 3.1 summarizes the different surface protrusions presented by Zdravkovich from his review of various means to suppress vortex shedding vibrations.

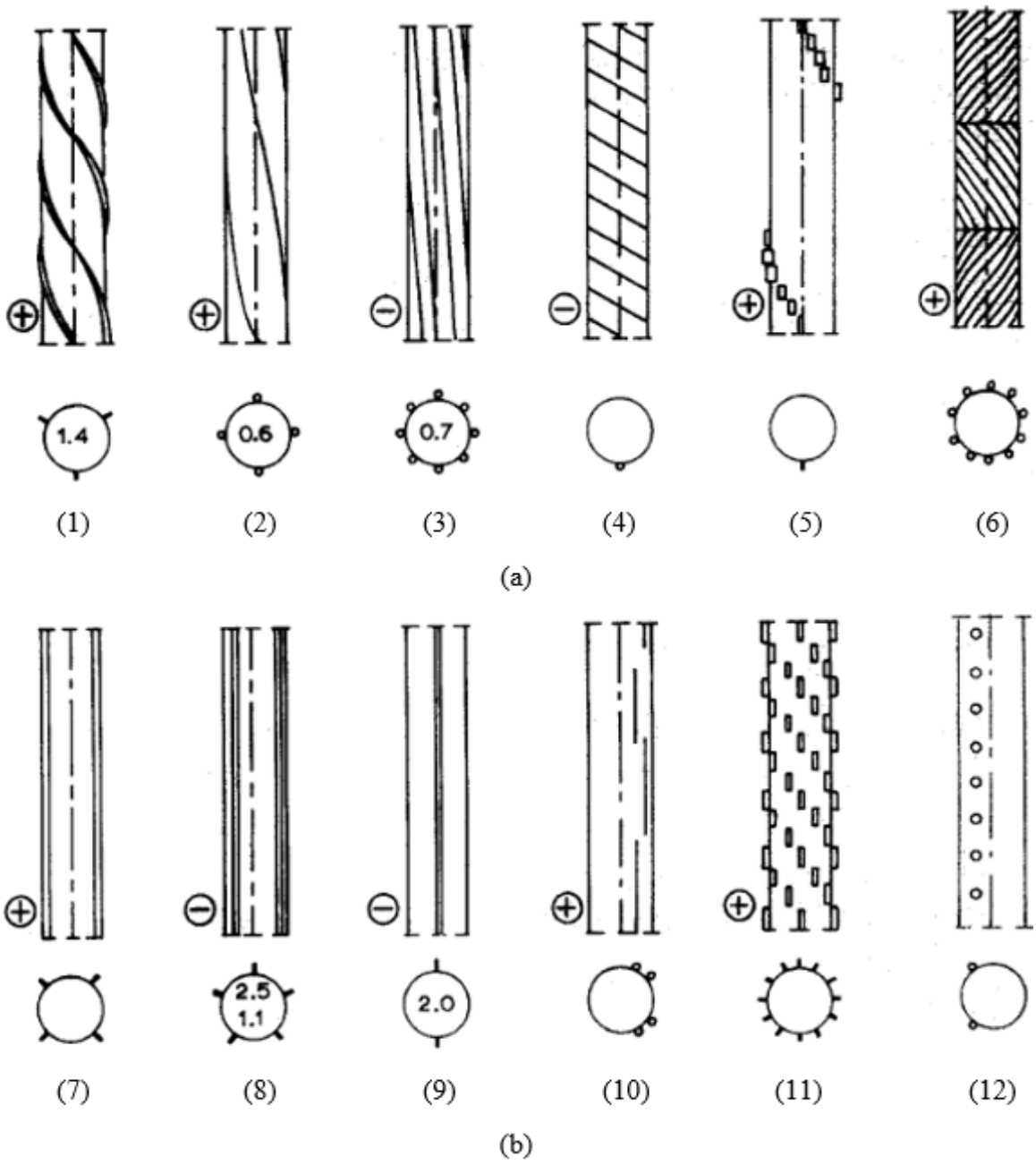

Figure 3.5 Surface protrusions: (a) omnidirectional, (b) unidirectional [17]

Table 3.1 Classification of surface protrusions [17]

Subdivision	Number	Name	Traits	Effectiveness
Omnidirectional	1	Strakes	Helical pattern	Effective
	2	Wires	Helical pattern	Effective
	3	Wires	Helical pattern - 8 wires	Adverse
	4	Wire	Helical pattern - one wire	Adverse
	5	Plates	Helix pattern - Rectangular	Effective
	6	Wires	Herringbone pattern	Effective
Unidirectional	7	Fins	X cross - 4 straight fins	Effective
	8	Fins	5 straight Fins	Adverse
	9	Fins	Symmetric	Adverse
	10	Wires	Staggered straight wires	Effective
	11	Fins	Rectangular and staggered	Effective
	12	Spheres	Turbulence promoters	Effective

As can be concluded from Table 3.1, any specific type of surface protrusion does not necessarily equate an effective method. The effectiveness of each protrusion type is highly dependent on the height to diameter ratio of the device, the pitch distance, the coverage percentage of the cylinder and the pattern.

For the rest of the discussion on surface protrusions, the focus will be directed towards helically patterned strakes for the purpose of this thesis in the study of spiral disruptions on high mast lighting towers.

Helical strakes (Figure 3.6) have been widely used in the industry for their proven ability to curtail vortex induced vibrations responsible for lock-in by affecting the shear layer. Kumar et al. have presented different patented helical strakes inventions that are both cheap and effective; however, these specific methods can adversely increase drag and are prone to biological marine accumulations when used in the marine industry. For chimneys and round stacks, an optimal design of a strake is one with a diameter of 10% the diameter of the structure and helically spaced with a pitch distance of 15D. Furthermore, the helical strakes do not need to cover more than 50% of the structure to sufficiently reduce vortex induced oscillations and prevent lock-in [13].

A wind tunnel experiment performed by Zhou et al. captures the vortex shedding phenomena in a bare cylinder and lack thereof on a cylinder equipped with helical strakes using a smoke flow visualization technique as shown in Figure 3.7. It can be clearly seen from the figure that the vortices have significantly subsided for the model with helical strakes. Zhou et al., in their study, have also found that a cylinder mounted with three-strand helical strakes with a height of 0.12D (D being the diameter of the cylinder) and

spaced with a pitch distance of 10D can reduce vortex induced vibrations by up to 98% and erase any traces of lock-in [19].

Some helical strakes have been found to successfully work in wind applications, and the same could be said when used as a hydrodynamic method. In such an application, Baarholm et al. performed a computational study on marine risers covered with helical strakes and simulated in both sheared and uniform currents. The researchers have found that the larger riser area fitted with the strakes, the better control of the vortex induced vibrations. However, the frequency response was highly dependent on the diameter of the strakes and the pitch distance at which they were installed [20]. A similar study on marine risers by Huang, has shown that a triple start helical groove configuration can decrease the oscillation amplitude of the vortex induced vibrations by up to 64%. This study was carried for helical strakes that have a height of 0.2D (D is the diameter of the cylinder) and a pitch ratio of 6 for a range of Reynolds numbers from 1.3×10^4 to 4.6×10^4 [21].

Chyu et al. adopted a Particle Image Velocimetry method used in an experimental water tunnel setup in their “Near-wake flow structure of a cylinder with a helical surface perturbation” study. The experiment consisted of a flexible wire in a three-start helical pattern with a diameter of 0.1D (D being the diameter of the cylinder) and a pitch distance between the sequential ridges of 1/3D. The strakes were glued to the model and submerged in a water tank with a flow velocity that yields a Reynolds number of 10 000. The results showed a complete obstruction of the formation of vortices in the wake region near the surface of the cylinder. Chyu et al. claim that “distinctive patterns of vorticity in

all three orthogonal planes in the near wake" are associated with the lack of vortex formation [22].

Figure 3.6 Stacks in Laramie, WY retrofitted with helical strakes [3]

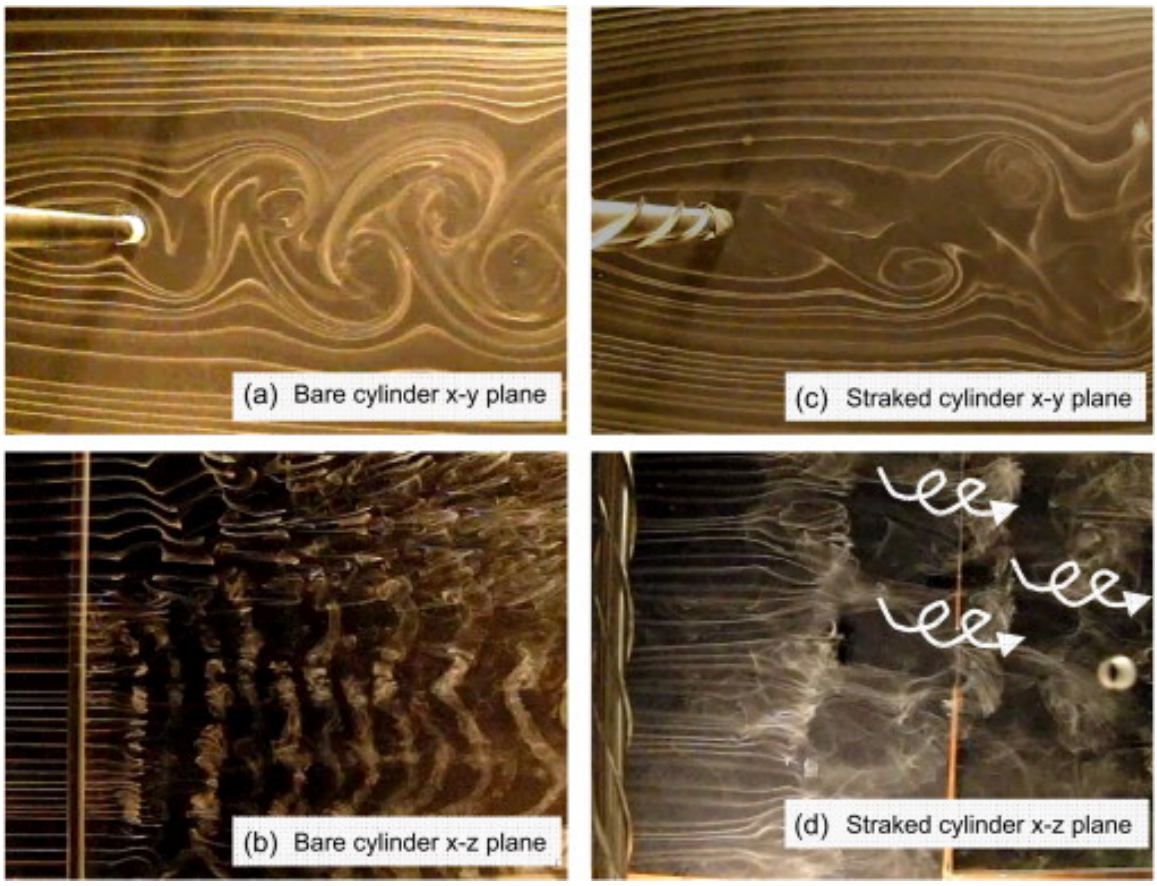

Figure 3.7 Wind tunnel smoke flow visualization of a cylinders wakes: (a) and (b) bare cylinder, (c) and (d) straked cylinder [19]

On the other hand, shrouds are thin hollow cylindrical perforated or slatted metal sheets that cover the model as shown in Figure 3.8 [13].

Shrouds are generally considered omnidirectional means that suppress vortex induced vibrations by affecting the entrainment layer [17], a concept defined earlier in the chapter. However, it has been found that for some designs where a shroud is incomplete, meaning only partially covering a cylinder, the latter becomes omnidirectional and can adversely affect structural vibrations and beyond double the fluid excitation [17].

Inventors have created perforated shrouds with circular holes capable of controlling structural vibrations as well as lowering drag. The shroud design consists of a thin cylinder with a diameter of 1.25D and a complete perforated area between 30% to 40% of the cylinder while only covering 45% to 55% of the cylinder area.

Generally, axial slats are designed to have a diameter of 1.3 times the diameter of the structure it encompasses and only cover 60% of the model. Although more effective than perforated shrouds at suppressing oscillations, axial slats are relatively more expensive than perforated shrouds and helical strakes and are generally used mainly in marine applications [13].

A full-scale experimental study was performed by Ahearn et al. for the State of Wyoming Department of Transportation, where two identical 120 ft. tall high mast lighting poles were retrofitted with different devices and their dynamic responses were monitored and analyzed. Both poles were equipped with helical strakes, ribbon dampers, perforated shrouds, and surface roughness at different times each. The first pole experienced lock-in at the 3rd mode and positively responded to the perforated shroud but none of the other devices. The perforated shroud was 16 ft. long covering approximately 13% of the structure near the top with a diameter of 1.25 the diameter of the pole at each location to match the taper of the original pole. The second pole was unresponsive to all devices due to its near location to the highway, where traffic was greatly affecting its structural response. Traffic induced vibrations were found to be the main cause of the largely different response of the pole. The retrofits did not affect the second pole, simply because the traffic induced vibrations prevented lock-in by exciting the structure at higher frequencies [3].

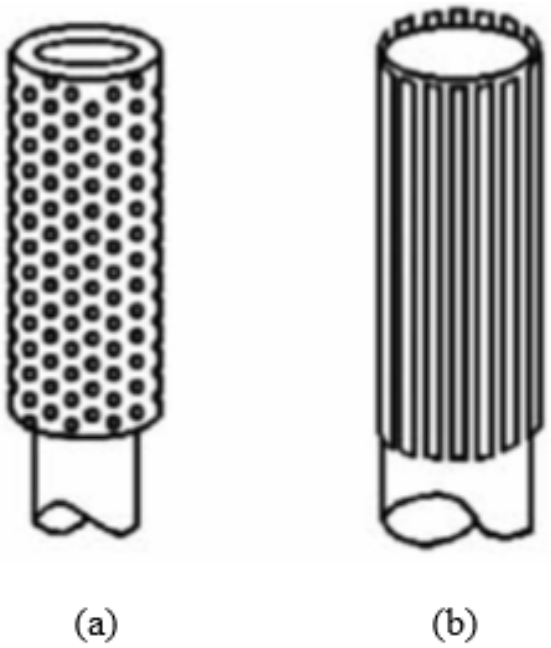

Figure 3.8 Shrouds examples: (a) perforated shroud, (b) axial slats [13]

Although extensive research has been performed to create effective means to suppress vortex induced vibrations and hence prevent the lock-in phenomenon from occurring, most of this research has been limited to plain cylinders and applied globally to different applications in marine and civil engineering including marine risers, cables, chimneys, and high mast lighting towers. Through this literature review, it can be concluded that a steep curve is still ahead of researchers and inventors in their attempt at creating more effective, cost efficient, and elegant solutions to the issues arising from vortex induced vibrations and lock-in. Unfortunately, there is no ultimate solution to the lock-in issue and each specific mean is highly dependent on the nature of the structure, shape of the structure, surrounding environment, and weather conditions to name a few. Many researchers have encouraged further studies for other structures including multi-sided and/or tapered slender structures.

CHAPTER 4. SETUP, PROCEDURES, AND DATA PROCESSING

This chapter describes the experimental setup, equipment, and procedures followed to collect and process the necessary data for this study.

4.1 Wind Tunnel

The subsonic Boeing wind tunnel located at the Aerospace Sciences Laboratory in the School of Aeronautics and Astronautics at Purdue University is used during the experiment to simulate wind flow and to control the flow velocity. The closed-return wind tunnel has a closed 4 ft. x 6 ft. test section that houses the model to be tested.

A schematic of the tunnel with the mounted model can be seen in Figure 4.1.

4.2 Models

Two multi-sided models have been used during the experiment. The HMLT scaled models have been constructed by Jaime Ocampo for his Ph.D. dissertation and used during this experiment. Each model has been manufactured using fiberglass foam core boards, wood spars, and extruded aluminum tubes. The aluminum tubes provide an opening for numerous vinyl tubes connected to pressure taps on the surfaces of the models. The HMLT models are 12- and 16-sided with a regular polygonal cross-section. Each model is 5 feet long with a diameter of 5 inches at the center (used as the characteristic length to calculate the Reynolds number) and a taper ratio of 0.14 in/ft. It is important to note that modeling scaling ratios for wind tunnel testing are typically 1:1 or

2:1. Here, with a full scale height of a tower ranging between 100 ft. to 160ft. and the available width of the wind tunnel test section, the tower scale ratio would be as high as 32:1. This high ratio complicates modeling a complete scaled high mast lighting tower model, thus only a partial section of the model has been manufactured and tested.

In order to remain consistent with Ocampo's measurement locations, data was collected at the same locations at which his data was collected. The purpose of these particular locations is due to the presence of pressure taps at said locations. The pressure taps were not used during this study due to the unviable pressure values recorded. There are a total of 17 measurement locations for the hot-wire probes for each model. These align with the pressure taps located 1, 2, 3, 8, 10, 12, 14, and 16 inches both left and right of the span-wise center of the model. The measurement locations towards the thin end of the model from the span-wise center are set as negative distances and the measurement locations towards the thick end of the model as positive values. A schematic of the 12-sided model with dimensions in inches as well as a visual description of the measurement locations is shown in Figure 4.2.

4.3 Tunnel Setup

Two aluminum airfoil extrusions slide through openings on the sides of the wind tunnel test section floor. The extrusions are attached to square metal bars around the perimeter of the test section floor using a linear roller. Each airfoil extrusion is secured at the bottom of the wind tunnel to a forcing mechanism that include clamps, springs, and linear bearings. For the purpose of this experiment, the extrusions are each attached to a steel shaft from the forcing mechanism that is clamped in place as seen in Figure 4.3.

Two aluminum tubes extrude from the sides of the model providing opening for the pressure tabs vinyl tubes. These tubes slide into hollow copper tubes on each end of the airfoil extrusion, holding the model in position as shown in Figure 4.4.

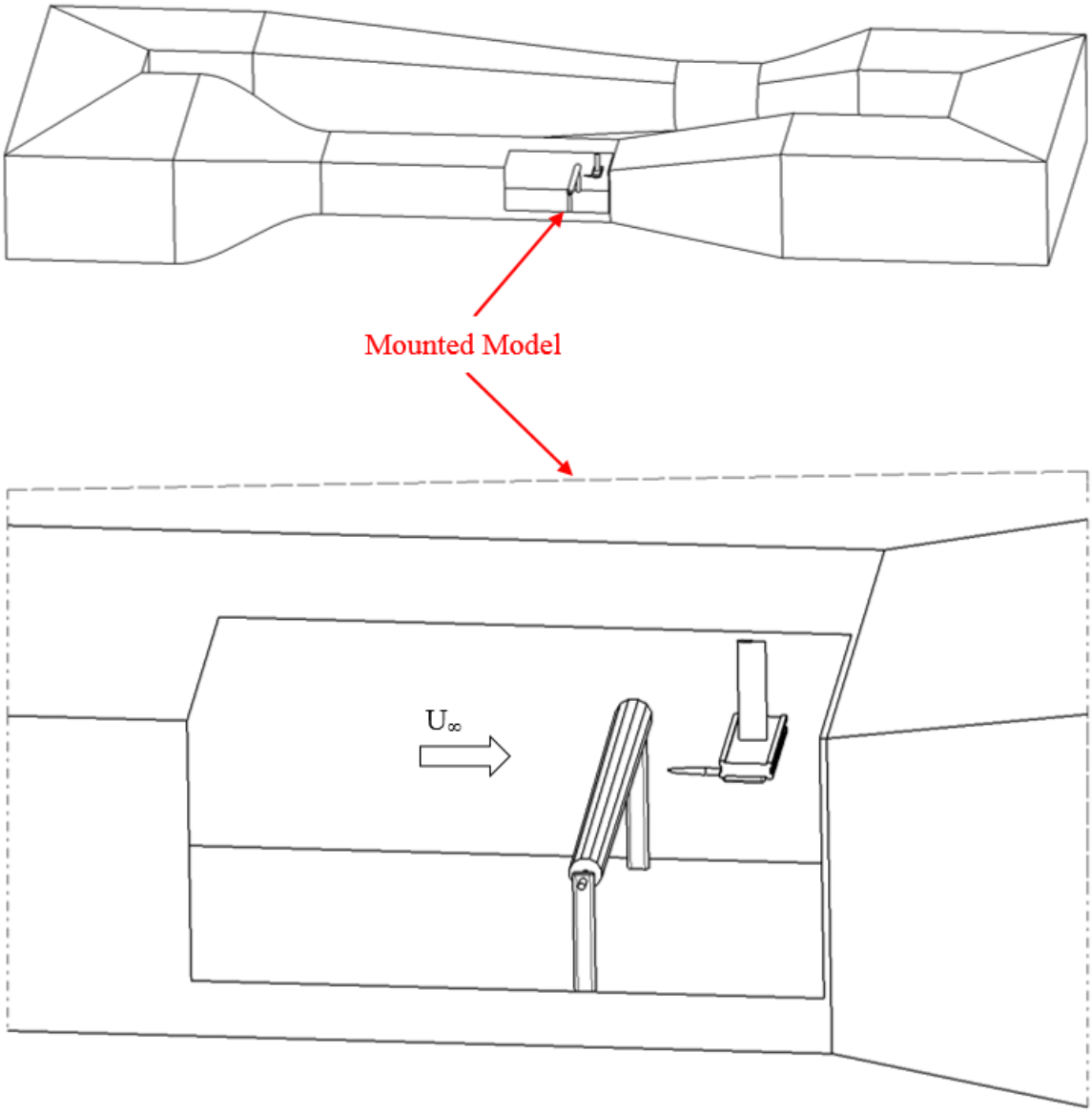

Figure 4.1 Boeing Wind Tunnel Schematic

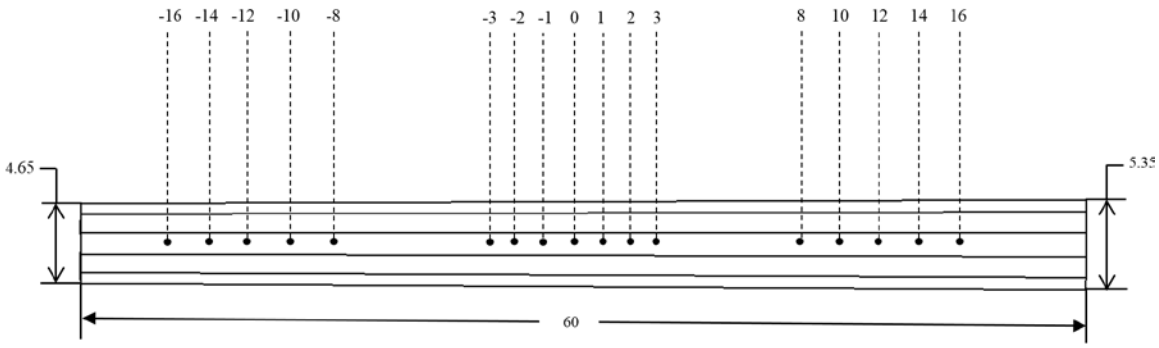

Figure 4.2 Pressure Taps Locations Schematic

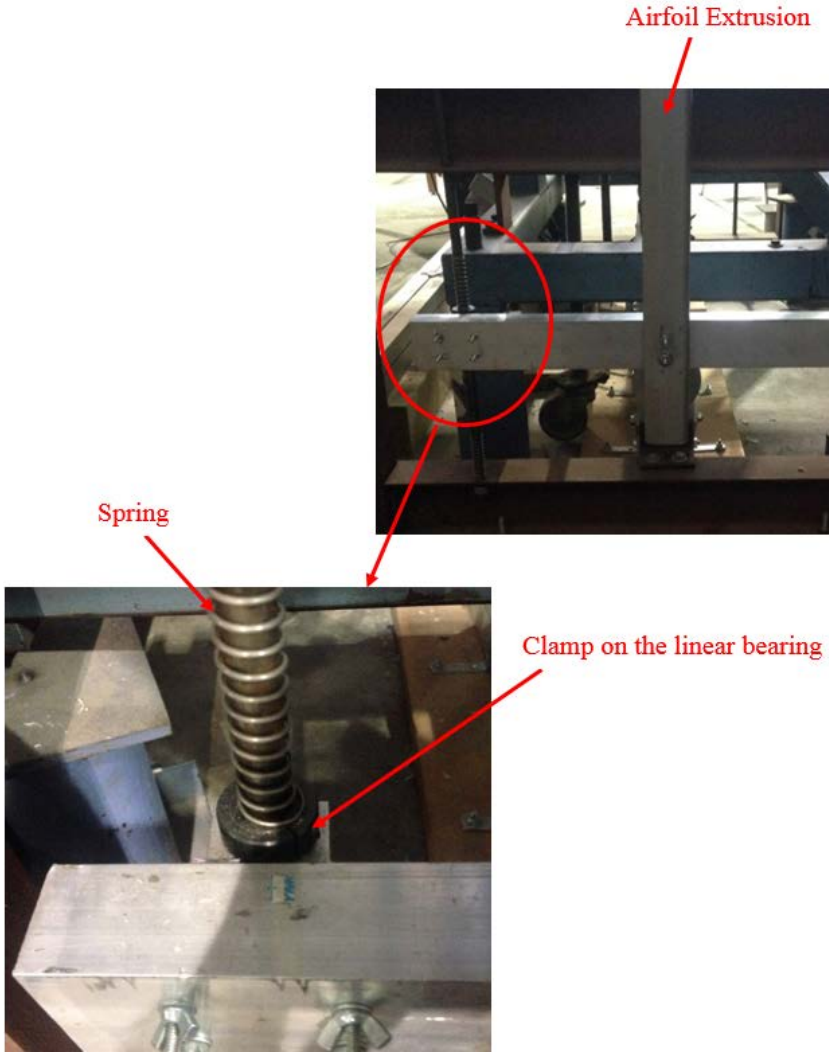

Figure 4.3 Holding System

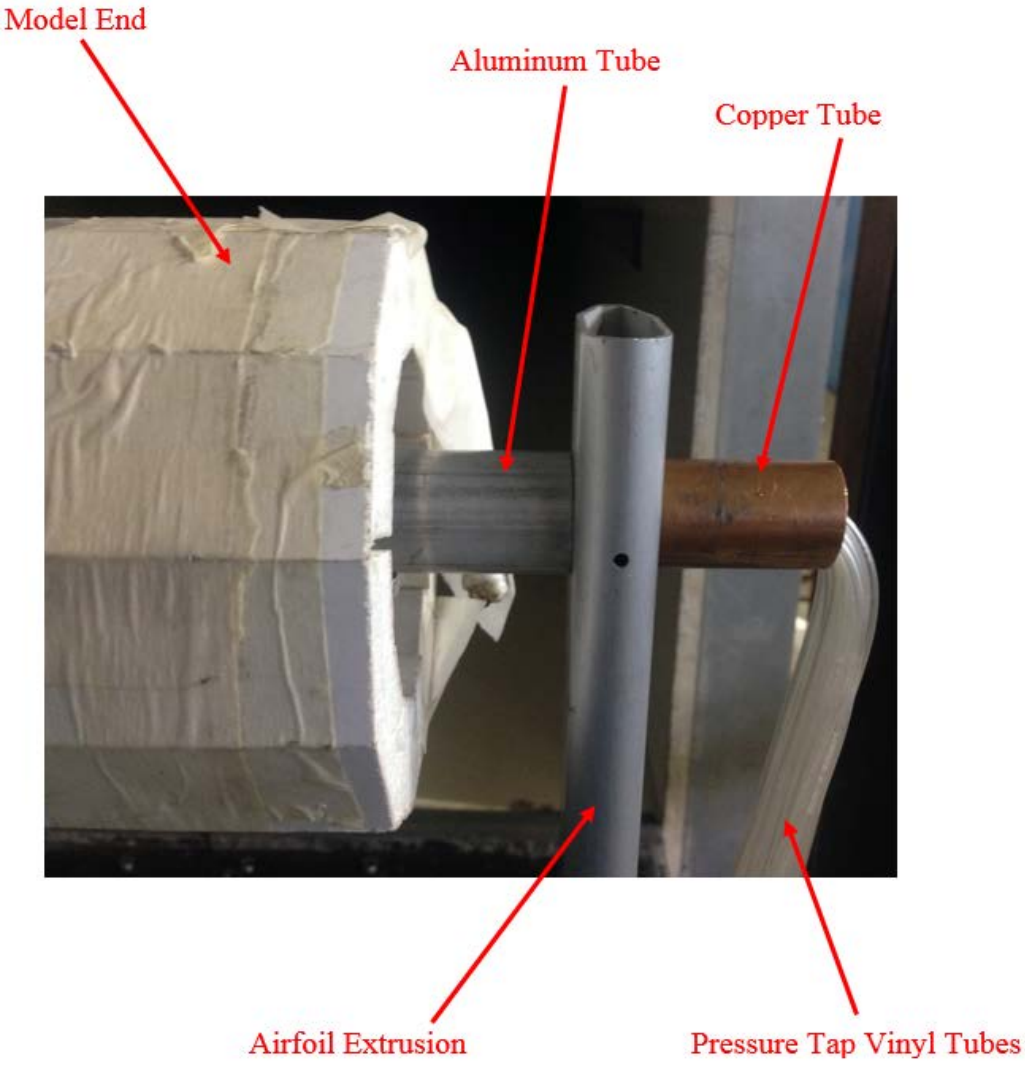

Figure 4.4 Model Setup

4.4 Model Configurations

The model, being oriented either face- or vertex- upstream, is rotated to the angle that would define its configuration as shown in Figure 4.5, where U_∞ is the free stream velocity. The model's position in the wind tunnel is assured using a level at the center of the model for repeatability purposes. A basic summary of the configurations is as follows: face-upstream is the configuration where one of the faces of the model is perpendicular to the free-stream flow direction; and vertex-upstream is when one edge connecting two faces in the model is facing in the up-wind direction. The face in the model containing the pressure tap ports was used as a reference point during the set up. The model is in the face-upstream configuration when the face fronting the wind direction is at angle of 90° from the reference face and the model is considered to have an angle of attack of $\alpha = 0°$. Meanwhile, the vertex-upstream configuration is attained when the edge facing the wind direction is 112.5° from the reference geometry with a model angle of attack of $\alpha = 22.5°$. The attained signal and thus the shedding frequency data varied in response to the changes in the angle of attack.

The two configurations were chosen due to the symmetric nature of the models and the ability to compare basic data with Ocampo's results from his PhD dissertation. Although only two angles are studied in the experiment, the change in the model's configuration provides some ability to perform "cross wind" studies in a wind tunnel setting and to study the shedding frequency differences between the two cases. Further angle of attack studies would have been lengthy but can be of interest in future work.

Previous work has been performed without a spiral disruption but the main purpose of this paper is to consider the flow field with a spiral disruption as a mean of mitigation of

wind-induced oscillations. Previous research on vortex induced vibration suppression suggests that an effective helical strake geometry for cylinders and long slender tubulars should have a strake-to-structure ratio of about one tenth of the diameter of the structure [1]. Two different rope diameters, a ¼ inch and ½ inch, were used during the study. Respectively, each rope is approximately 5% and 10% the size of the average diameter of the scaled model. The ropes were wrapped around the model in a helical pattern. The wrappings were spaced equally across the model at intervals of 7.5 inches for a total of 8 revolutions. The pitch distance was chosen arbitrarily given that enough strakes were wrapped around the model along its length. In order to keep the rope in position, the rope was secured to the backside of the model by using duct tape and marking the position of the rope for repeatability purposes. An illustration of the rope pattern is shown in Figure 4.6.

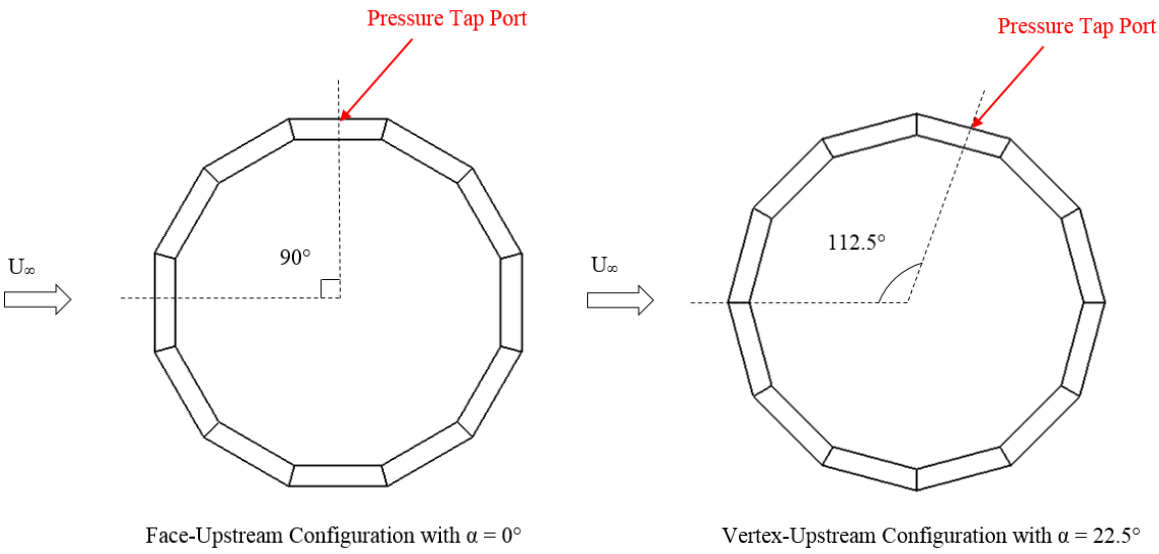

Figure 4.5 Model's Angles of Attack

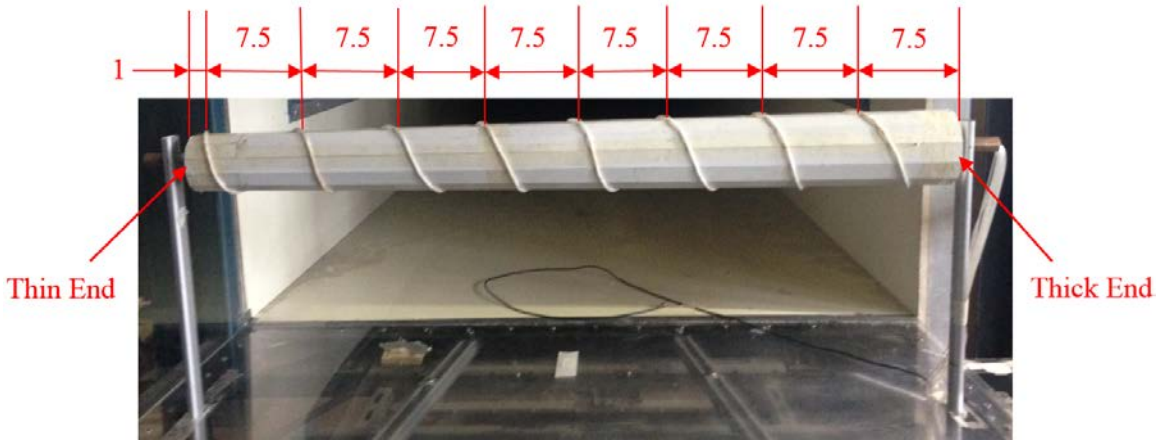

Figure 4.6 Spiral Disruption Configurations

4.5 Data Acquisition System

A set of instruments is used to collect data and monitor the voltage output. The instrumentation includes a hot wire sensor with a traversing mechanism, a multimeter, an anemometer, and an oscilloscope.

The hot wire sensor is a useful tool in providing a way to measure voltage and flow velocity. Heat is generated when a current passes through a very thin gold or platinum-plated wire in the sensor. When placed in a flow stream, the wire's temperature changes from the heat transfer between the wire and the flow. The amount of transferred heat between a hot wire and the flow stream is directly related to the magnitude of the voltage passing through the wire required to keep it a constant temperature. King's Law, defined by Equation (4.1), is an empirical formula that relates V, the voltage applied to the wire and U, the fluid velocity. This formula is useful in measuring the flow velocity and calibrating the hot wire.

$$\sqrt{U} = AV^2 + B \tag{4.1}$$

Figure 4.7 shows the hot wire mounted to a traversing mechanism through a hot wire probe support and two perpendicular 80/20 beams. The probe support is attached to the beam using a clamp and can slide through the T-slotted beam to the desired location. The traverse system is moved using a P315X stepper motor driver/indexer control and a motor. The traverse is held in position by a vertical brake controller that can be disengaged when the mechanism is ready to move. The travel path of the traverse is controlled through a LabVIEW program in a computer that communicates with the P315X. A serial port is connected to the P315X RS-232 port using a RS-232 to USB converter. The following port settings and format must be set for the communications mode:

- Bits per second: 9600;
- Data Bits: 8;
- Parity: None;
- Stop Bits: 1;
- Flow Control: None.

The hot wire sensor used to measure the data during the experiment is connected to a TSI IFA-100 Constant-Temperature anemometer using a BNC cable. The anemometer controls the resistance and the voltage of the sensor required to keep it a constant temperature due to the transferred heat between the hot wire and the flow while supplying energy.

The anemometer settings should be set correctly to avoid reading noisy, oscillating, or inaccurate data. The back panel of the anemometer provides an option to select either a 15 or 60 ft. cable length with an internal slide-switch. The shorter cable length was

selected in order to minimize signal loss within the cable with a 15 ft. standard RG58A/U, 50-ohm coaxial cable. The operating resistance and Bridge Compensation controls of the anemometer were set at predetermined values in order to optimize the frequency response of the anemometer. The operating resistance is computed by multiplying the sensor's cold resistance by 1.3. The cold resistance of the hot wire sensor can be measured by either reading the "Resistance Measure" value on the front panel of the anemometer or by using a multimeter. Both instruments were used to verify that the correct cold resistance of the sensor was measured. A value of 35 for the bridge compensation was selected according to the wire type from the anemometer operating manual in order to tune the frequency response.

The output voltage signals from the anemometer are sent to a Lecroy WaveJet 314A oscilloscope to monitor the signal and store the voltage data. The saved data is later processed to generate frequency spectra and to extract the shedding frequencies. The oscilloscope settings were set to collect 1000 samples per second for a record length of 100 seconds to acquire data well near the frequencies of interest, typically less than 20 Hz. An AC coupling was chosen in order to get enough resolution on the oscilloscope digitization and a resolution value is set according to the signal height in Volts per division for a total of 8 divisions.

The data acquisition system used to collect the hotwire data is shown in Figure 4.8.

A collection of ambient condition information is collected using the panel near the wind tunnel. Before and after each set of experiment, the following information is recorded to accurately measure the free stream velocity and Reynolds number: ambient temperature, ambient pressure, and the difference between total and static pressures.

During the experiment, the flow is considered inviscid and incompressible. Thus, Bernoulli's equation becomes useful in determining the average flow velocity. The information collected using the panel is used to measure the free stream velocity using Bernoulli's equation as follows:

$$\boldsymbol{P_s + \frac{1}{2}\rho U_\infty = P_t} \tag{4.2}$$

where U_∞ is the velocity, ρ is the flow density, P_s is the static pressure, P_t is the total pressure, and $\frac{1}{2}\rho U^2$ is the dynamic pressure.

Using the total and static pressure difference reading from the panel, Equation (4.2) can be manipulated in the form of the following equation to estimate the flow velocity:

$$\boldsymbol{U_\infty = \sqrt{\frac{2(P_t - P_s)}{\rho}}} \tag{4.3}$$

The air density is easily computed using the Ideal Gas Law $P = \rho RT$ from the ambient pressure P, the ambient temperature T, and the specific gas constant R.

The wind tunnel velocity can be measured using Bernoulli's equation. The free stream velocity is in turn used to compute the Reynold's number as described in Equation (2.2). An example of a Reynolds number sample calculation can be seen in Appendix A.

The overall setup of the experiment with the model installed in the wind tunnel and instrumentation can be seen in Figure 4.9.

Figure 4.7 Hot-Wire Set Up

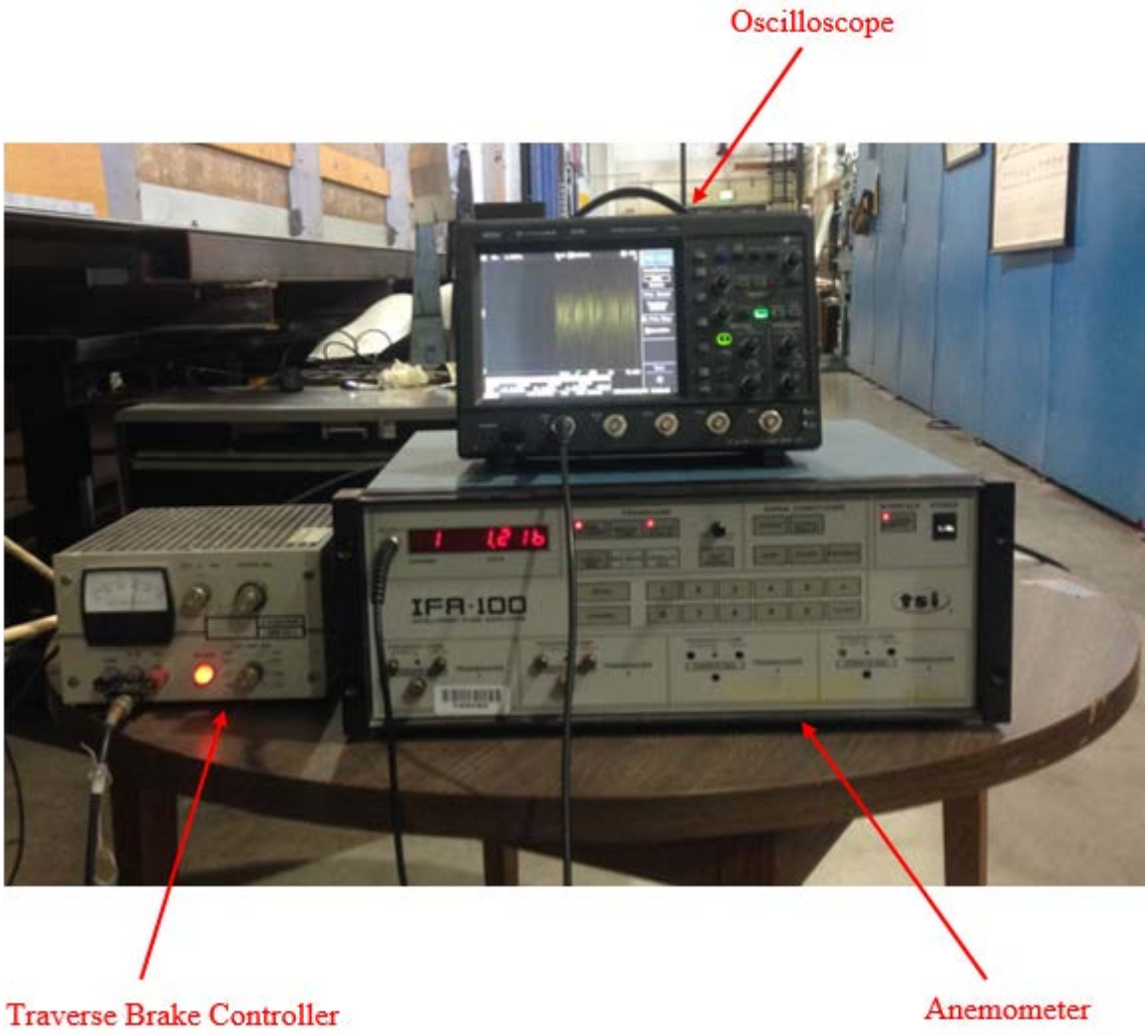

Figure 4.8 Data Collection Instrumentation

Figure 4.9 Overall Experimental Set up

4.6 Experimental Procedure

The following steps describe the experimental set up procedures and data collection methods:

1. Set up the model in the wind tunnel as described in Section 4.3.
2. Launch LabVIEW in the computer located near the Boeing Wind Tunnel and follow the next steps:
    a. Start the “7HPSurvey_SSBJTask7a_work_R6” vi code for the traverse driver.
    b. Run the vi code but do not disengage the break until the traverse has been initialized in order to avoid dropping the traverse.
    c. On the “Settings” tab, select the appropriate COM port under the P315x Traverse drop down menu and enable. The COM port is the port used for the RS-232 to USB converter as described in Section 4.5.
    d. Initiate the traverse.
    e. Disengage the break by switching the knob on the traverse brake controller power supply from “off” to “v”. A faint click should be heard when the break has been disengaged. If the click is not heard, the control knob for the output current should be set a higher value until the output voltage reaches the intended setting.
    f. On the “Main” tab, enter the desired value of the location of the traverse on the “Move To” cells. The top cell is used for the vertical position of the traverse with positive values moving the traverse down. Conversely, the bottom cell is used for the horizontal positioning of the traverse with

positive values moving the traverse right. It is important to note that the opening through which the traverse can move is only 24 inches wide and hence a value of 11 inches either to the left or to right should be set as the maximum value.

3. Set up the data acquisition system as follows:
    a. Install the hot wire probe on the traverse and connect it to a BNC cable.
    b. Connect the hotwire probe BNC cable to the input connector for a standard probe on the back panel of the anemometer. Set the Sensor switch to “wire” and the Bridge Selector switch to “Std 2”.
    c. Connect a BNC cable from the anemometer’s output connector on the front panel to the Channel 1 input connector on the oscilloscope.
    d. Carefully install a hot wire sensor on the hot wire probe. It is important to gently handle the hot wire sensor as it fragile and can easily be damaged.
    e. Turn on the anemometer and oscilloscope and set the control and setting values described in Section 4.5.
4. Tape any openings within the test section and close the tunnel door. Turn on the wind tunnel and adjust the tunnel frequency to the desired velocity.
5. Run the anemometer and adjust the settings on the oscilloscope and anemometer until a clear signal can be seen on the oscilloscope screen. The settings for the anemometer and oscilloscope should be set as described in Section 4.5.
6. Once a clear signal is attained, run the signal for the required length of time (100 seconds for this experiment) until the full horizontal width of the screen on the oscilloscope has been filled.

7. Copy the data from the oscilloscope onto a flash drive.
8. Move the traverse to the next location and save the new data.
9. The traverse can only move 11 inches to one side at a time, thus the experiment must be stopped halfway through each set to move the hot wire probe. Once the data is collected for one half of the model, the wind tunnel is turned off and the anemometer is put on standby. The hot wire is removed from the probe that then is placed in a new location on the 80/20 beam. The hotwire is placed back on the probe and the data collection procedure is repeated from steps 4 through 7.

4.7 Testing Configuration

In order to effectively study the effect of a spiral disruption on HMLTs, every set of experiment was performed on a clean model and on a model with spiral disruptions. The 12- sided model was tested using both the ¼ inch diameter rope and the ½ inch diameter rope and the 16-sided model using the ¼ inch diameter rope.

A total of 10 different configurations were tested, designed to capture the full spectrum of the study. The configurations under which the experiment was tested are tabulated in Table 4.1.

Table 4.1 Testing Configurations

Model	Disruption	Setup
12-Sided	None	Face Upstream
		Vertex Upstream
	¼ inch Diameter Rope	Face Upstream
		Vertex Upstream
	½ inch Diameter Rope	Face Upstream
		Vertex Upstream
16-Sided	None	Face Upstream
		Vertex Upstream
	¼ inch Diameter Rope	Face Upstream
		Vertex Upstream

To ensure reliable data, each test was conducted a total of three times to verify the repeatability of the experimental results. Two sets of the same tests using an identical configuration was repeated on the same day to compare results under similar ambient conditions including temperature and ambient pressure as well as having the model placed at the exact location. The third set of tests was repeated on a third day under varying conditions. A comparison of the repeatable results is shown in CHAPTER 5.

4.8 Data Processing

During the experiment, the data points collected from the hot-wire are displayed on one of the oscilloscope's channels. A screenshot of the raw experimental data is carefully collected and stored from the oscilloscope using a USB drive for further processing. The data is processed, using the MATLAB codes presented in Appendix B, through a series of steps summarized in the flowchart shown in Figure 4.10. Each step is described in the following two subsections.

4.8.1 Data Extraction

The raw data file is originally saved as an array of voltage vectors in its original time domain as a "csv" file. A MATLAB built in function named "csvread" is used to extract the formatted data file and to import it into a MATLAB friendly format. The data is then saved and stored within the software as described by the "Read_Data.m" section of Figure 4.10.

4.8.2 Data Filtering

The primary step in processing the saved data is the filtering of any unwanted noisy data that could potentially overshadow the frequency values of interest. This procedure is performed to clarify the signal before using an FFT (Fast Fourier Transform). The

filtering process consists of the following steps: subtracting the mean voltage, windowing, zero padding, and convolution.

First, the mean voltage value is subtracted from the data set to discard of the first and highest peak near “0”. This simple technique allows any other prominent peaks to be visible when looking at an FFT. Next, a cosine window is applied to the zero-mean data. A signal acquired from an oscilloscope is by nature artificially infinite and the endpoints are not connected. The discontinuity of the end points can appear as significant peaks in the signal, a phenomenon known as spectral leakage. Applying a window allows the signal to become a finite continuous one that can be transformed using the Fast Fourier method. Following the windowing step, zero padding is next applied to the signal. Zero padding is the action of adding a vector of zeros to the end of the time domain signal in order to lengthen the vector for smoother FFT spectra. The final step in the signal filtering process is the convolution of the zero-padded voltage vector with a “[1, 1]/2” vector using the built-in MATLAB function “conv” in order to smooth the signal. At this point, the original signal has been filtered and smoothed and is ready for the FFT.

4.8.3 Fast Fourier Transform

An FFT function is used to transform the time domain voltage vector into a frequency domain depiction of the signal. This step allows a clear visualization of the dominant frequencies in a signal spectrum. A “max” function is used in the MATLAB code to specifically pick the highest possible peak value in the FFT, which in most cases is the shedding frequency value. However, in some cases, a stronger peak at approximately 60 Hz overshadows the authentic shedding frequency peak. In experimental settings, hot-wires can act like an antenna that senses naturally occurring frequencies in the

environment, one of them being conveniently located around 60 Hz. The “max” function is unable to discern between the shedding frequency value and the “60 Hz” peak and the latter is discarded by generously cutting any data after a set mark of 50 Hz. Doing so allows a safe read of the true shedding frequency value. One example of a stronger 60 Hz peak and a 50 Hz post-cut FFT can be seen in Figure 4.11.

4.8.4 Peak Area and Width

After extracting the shedding frequency value and its location, a preset band of 1000 indices around the shedding frequency peak is used to create a bandwidth. The limits of the bandwidth are used to compute the area of the shedding frequency peak range using the MATLAB built-in function “trapz”. Finally, the peak’s width is computed by using the previously found area of the shedding frequency range and the height value of the peak.

Figure 4.10 Data Processing Flowchart

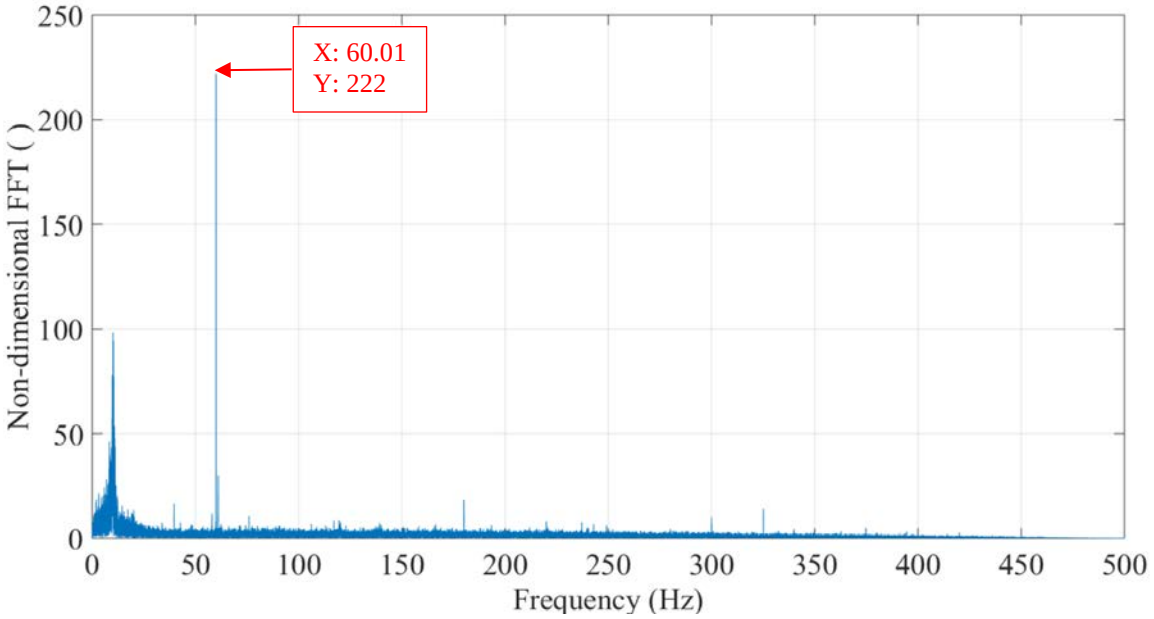

(a)

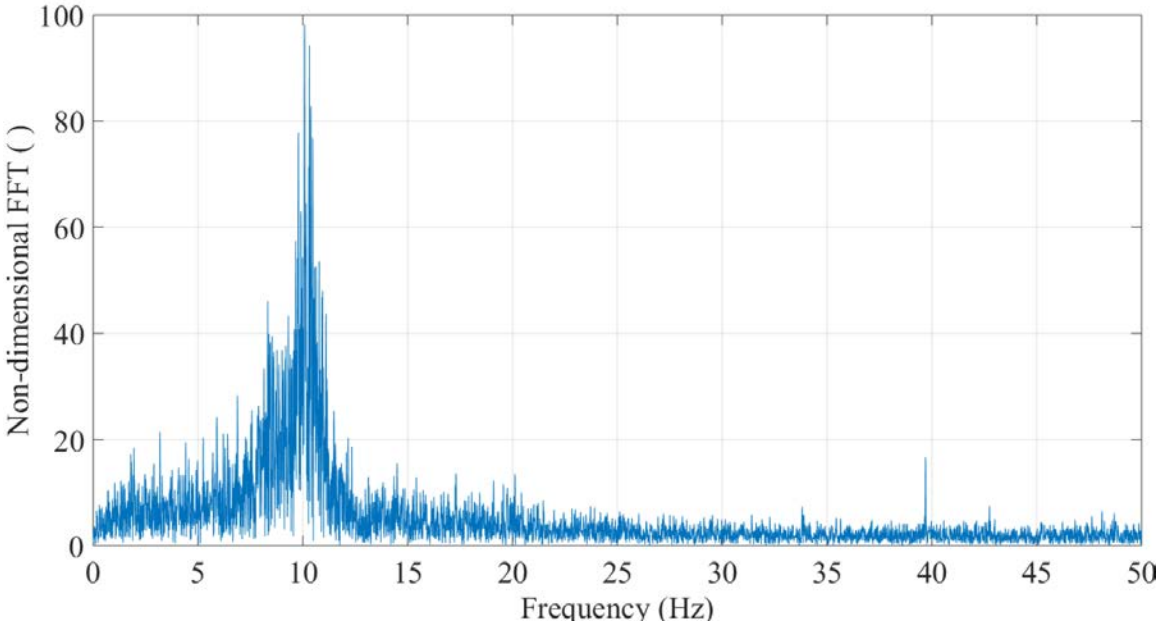

(b)

Figure 4.11 FFT example: (a) FFT with prominent 60 Hz peak, (b) FFT with data cut after 50 Hz

CHAPTER 5. RESULTS AND ANALYSIS

This chapter consists of 7 major sections that investigate the effects of different helical strakes configurations on the vortex shedding lock-in phenomenon of a 12- and a 16-sided tapered HMLT models.

First, a cross-wind study is reviewed and a noise sensitivity study is examined. Next, the preliminary frequency responses of the models are analyzed and a sample of FFT signals is explored. Furthermore, a total number of four distinct aspects of the signals are studied. The additional aspects that are being revised are as follows: signal strength, peak area, and finally the peak width.

5.1 Cross-wind Location

A cross-wind study was performed by Ocampo in his dissertation to measure the characteristic frequencies in the cross-wind location of the HMLT models. The test included the 8-, 12-, and 16-sided scaled models, clamped in place, under the same average Reynolds number. The reason behind such a study is to locate the transitional area between the oscillation driven shear layer and the separated flow in the near wake. Figure 5.1 presents the results of the cross-wind study that clearly shows that a distance greater than one diameter away from the center of the model is the ideal area to capture the shedding frequencies in the oscillating shear layer. Any distance less than one diameter will produce unreliable results from the separating flow around the models [2].

Because of the concluding remark from the cross-wind test results, a distance of 1.5 D (D being the characteristic diameter of the models) from the center of the model was chosen to reliably capture the shedding frequencies of the vortices. The distance between the hot-wire sensor and the center of the model measures to 7.5 inches from assuming a constant model diameter of 5 inches. A schematic of the configuration can be seen in Figure 5.2.

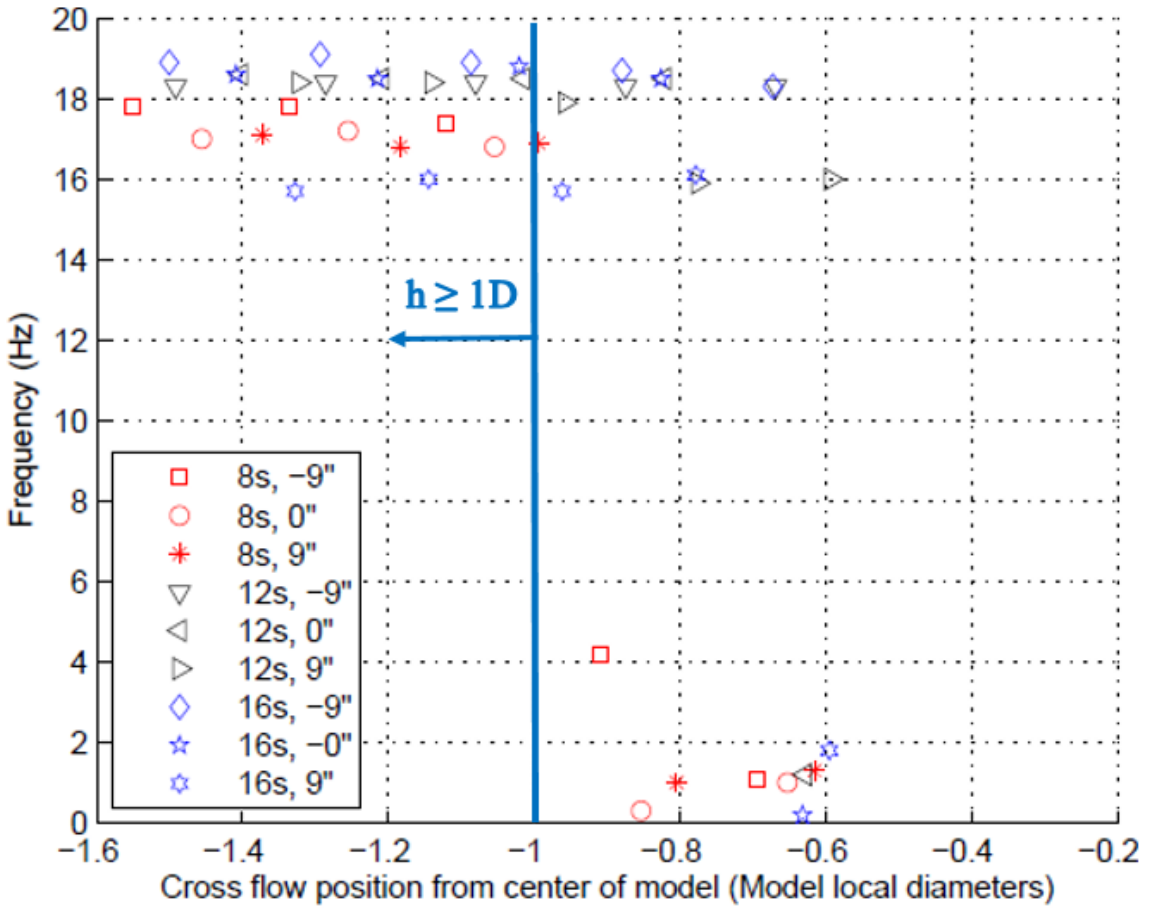

Figure 5.1 Characteristic frequencies of the 8-, 12-, and 16-sided models at the cross-flow position [2]

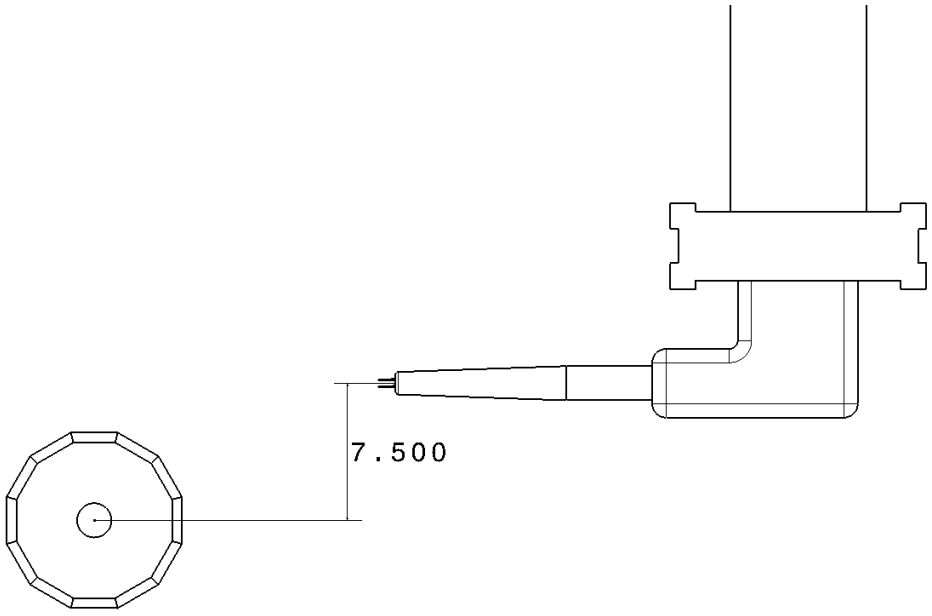

Figure 5.2 Distance between the hot-wire and the center of the model

5.2 Noise Sensitivity

One of the steps in the signal filtering process is the convolution of the data with a simple discrete vector. Convolution is the product of two functions or signals, which demonstrates the shape effect of each signal. Under the assumption that the acquired original signal from the scope is a combination of the signal of interest and noise, convolving the signal with a vector allows a clearer representation of the signal and a better control of the noise sensitivity within said signal when performing an FFT. The vector used for a convolution process is a simple two by one matrix of ones as follows: [1, 1].

A good visual of the signal to noise ratio effect can be seen in Figure 5.3. The top graph is the resulting FFT from a convolution of the data with a [1, 1] vector, while the bottom graph is with a [1, 1, 1, 1] vector convolution. The lack of change in the FFT suggests

that the length of the vector used while convolving does not affect the representation of the signal. Hence, the noise sensitivity of the signal is considered low enough that a shorter vector is sufficient while performing the convolution step in the filtering process and the disposing of noisy data that clouds the signal of interest.

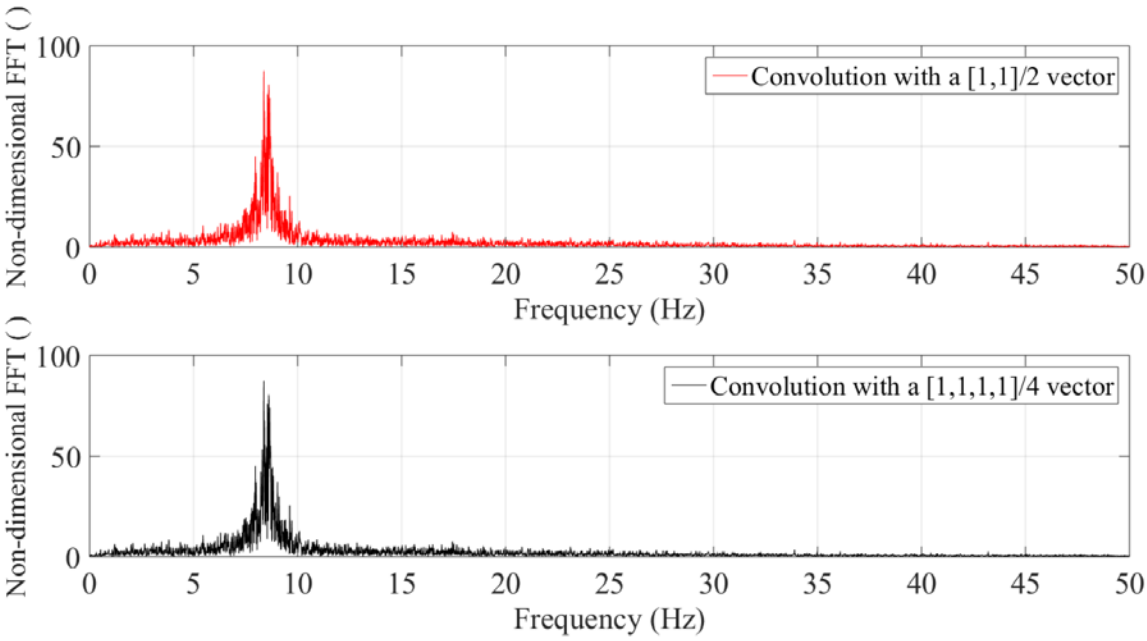

Figure 5.3 Convolution changes

5.3 Shedding Frequency Measurements

The following section presents the original findings of the experiment from the collected hot-wire data. The first aspect of the FFT that is examined is the characteristic vortex shedding frequency. In this section, the shedding frequency measurements are expressed in terms of Strouhal values from taking into account variations in the Reynolds number due to environmental changes. The Strouhal numbers are computed using the non-dimensional Strouhal relation, from Equation 2.3, expressed in terms of the shedding frequency and the Reynolds number. Initially, the repeatability of the experimental

results is inspected to verify if any unwanted changes from the surroundings or the experimental set-up affect the outcome of the tests. Furthermore, the shedding frequencies by means of Strouhal values of the 12- and 16-sided model in both the face and vertex upwind configurations, with and without a helically patterned strake retrofit, are analyzed. The data is collected at an average Reynolds number of 44,000 for all cases. In order to effectively study the effect of the helical strakes on the HMLT models, both a "bare" configuration of the models without any retrofits, and a "helical strake" configuration is tested. The results from all configurations are compared and analyzed. As described in the setup and procedures section, the 12-sided model is equipped in two different cases with a ¼ inch and ½ inch diameter rope, denoting 5% and 10% of the diameter of the model respectively. On the other hand, the 16-sided model retrofit includes a ¼ inch diameter rope disruption configuration. The pitch distance of the helical strakes measures 7.5 inches or 1.5D, with D being the "center" diameter of both models. The rope for each case is installed along the full length of the model.

In this section and all subsequent sections in the results chapter, the measurement locations range from 1 inch to 16 inches both left and right of the span-wise center of the model. The negative values in the locating x-axis represent a direction towards the thin end of the model, while the positive locations converge to the thick end of the model.

5.3.1 Repeatability

All hot-wire measurements were repeated and collected for the same configurations a total of three times. The test was repeated twice during the same day under similar ambient conditions including temperature, ambient pressure, and identical model position. The third set of tests was conducted on a different day under different ambient

conditions. The triple data collection is carried out to ensure the repeatability of the experiment irrespective of the environmental conditions.

Due to the large size of the collected data, a random sample of cases has been chosen to attest to the overall repeatability of the experiment. The four presented sample cases, as seen in Figure 5.4 through Figure 5.7, are as follows: bare 12-sided model in the face upwind configuration, bare 16-sided model in the vertex upwind configuration, 12-sided model with a ½ inch diameter rope strake in the vertex upwind configuration, 16-sided model with a ¼ inch diameter rope strake in the vertex upwind configuration. From the repeatability figures, it is observed that the Strouhal values from the shedding frequencies at the locations across the length of the model are very similar, indicating a good experimental repeatability. Some slight value differences can be seen towards the thicker end of the model at locations 8 inches to 16 inches from the center of the model. These minor differences can be attributed to larger fluctuations, such as temperature or pressure, near that side of the model. However, the variance is small enough to be considered negligible and would not affect the main concluding outcome of the results.

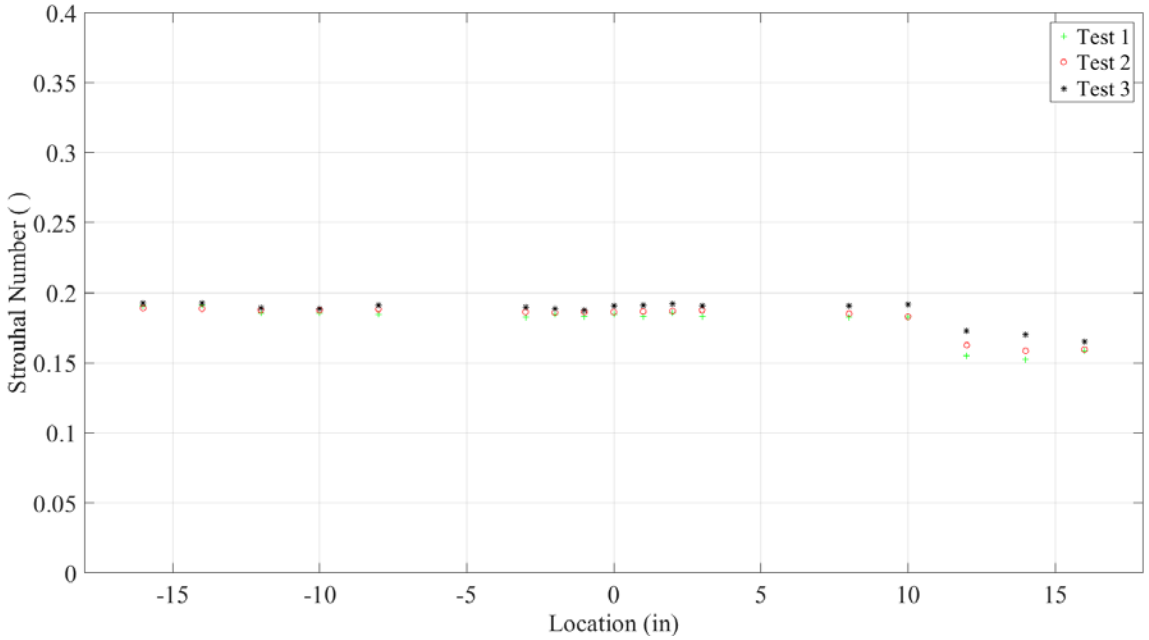

Figure 5.4 Repeatability of the bare 12-sided model in the face upwind configuration at Re = 44,000

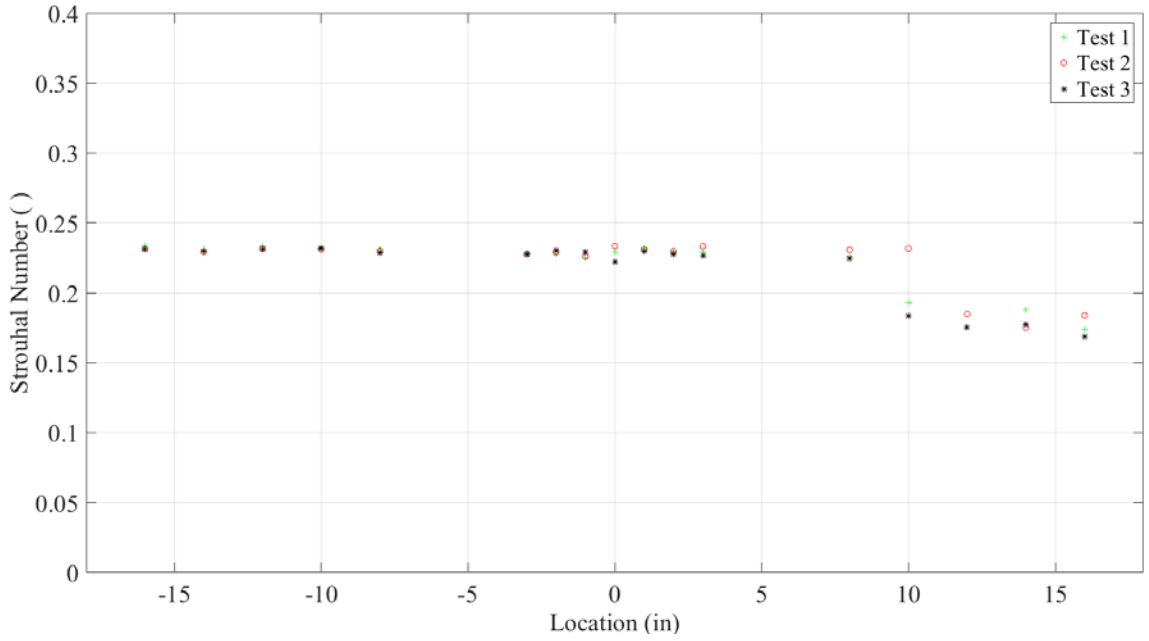

Figure 5.5 Repeatability of the bare 16-sided model in the vertex upwind configuration at Re = 44,000

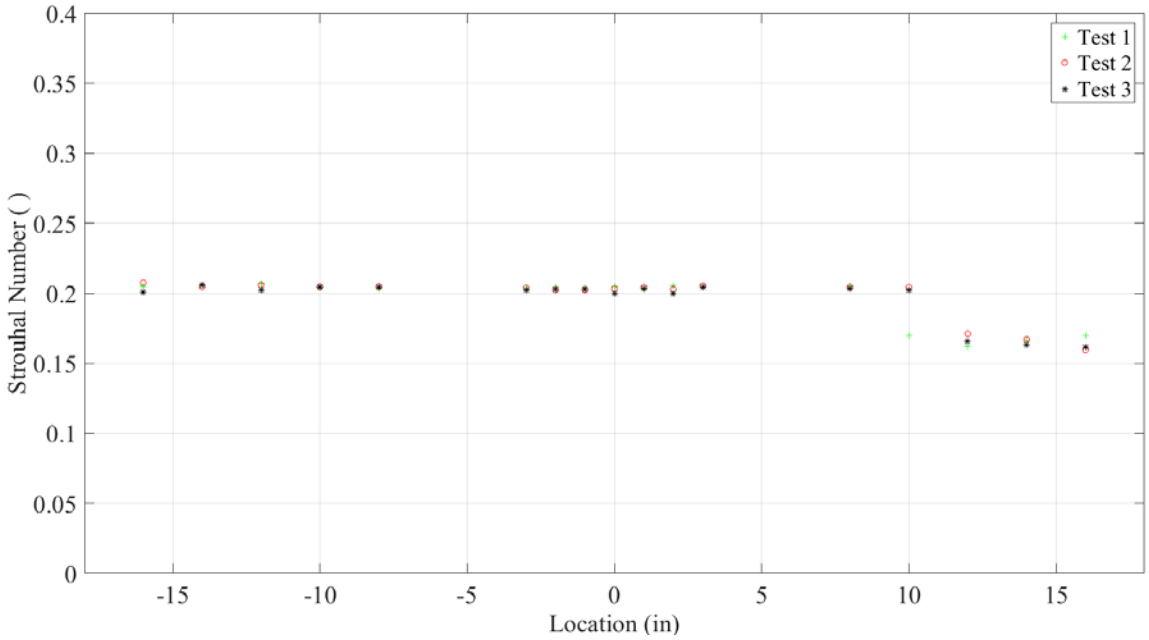

Figure 5.6 Repeatability of the 12-sided model with a ½ inch diameter rope strake in the vertex upwind configuration at Re = 44,000

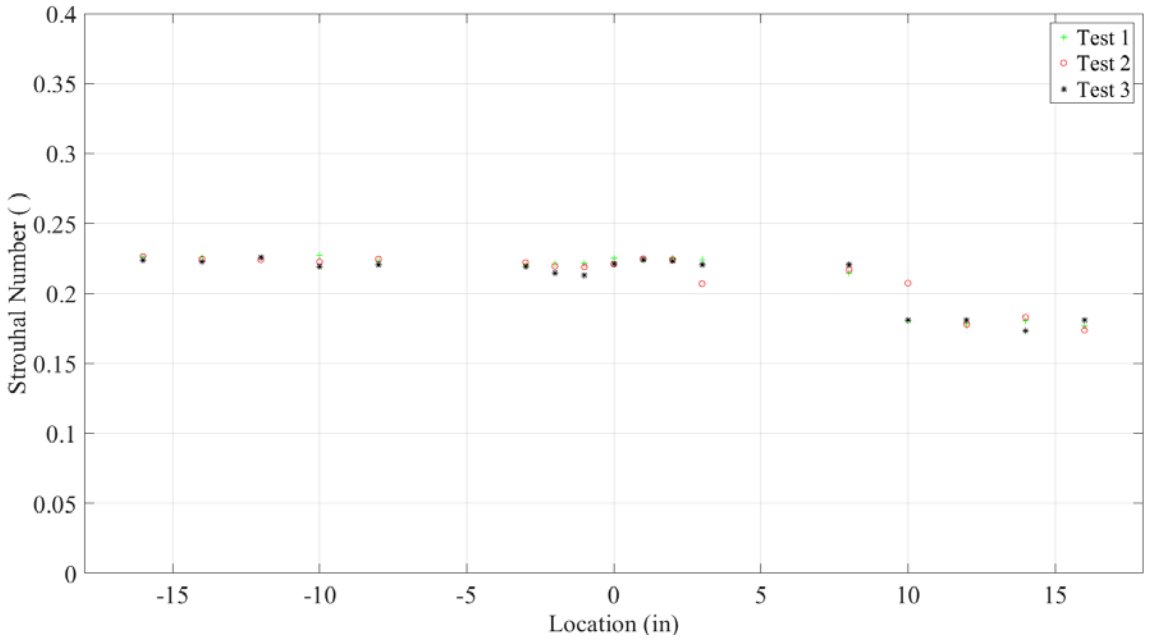

Figure 5.7 Repeatability of the 16-sided model with a ¼ inch diameter rope strake in the vertex upwind configuration at Re = 44,000

5.3.2 12-Sided Model: Shedding Frequency Study

The Strouhal numbers of the 12-sided model in the “bare”, “¼ inch diameter rope helical strake”, and “½ inch diameter rope helical strake” arrangements are compared in Figure 5.8 and Figure 5.9. The former presents the results in the face upwind configuration while the latter is in the vertex upwind configuration.

Contrary to the initial expectation of the effect of the rope strakes, Figure 5.8 does not show any significant changes between the bare and straked 12-sided model in the face-upwind configuration. However, the pronounced proximity of the Strouhal values, at various diameter measurement locations, is indicative of the lock in phenomenon. The stronger peaks are identified near the thinner end of the model (x = -16 to x = -8 inches). This remark could be attributed to the model being slenderer and hence more prone to larger amplitude vortex induced vibrations. Figure 5.9 also shows an apparent vortex shedding lock-in occurrence in the vertex upwind configuration for the bare and fitted cases. However, unlike the face upwind orientation, an overall shift (both upward and downward) in the frequency peaks is observed when the rope is applied to the model. The ½ inch diameter assists in an amplitude decrease of the shedding frequency values and brings them closer to the face upwind results. Conversely, the ¼ inch diameter adversely contributes to a slight hike of the shedding frequency values.

It is also interesting to note that the characteristic shedding frequencies in the vertex upwind configuration are generally larger in amplitude than their face upwind counterparts. An early separation from the sharper edge of the model may be responsible for the increased frequency values at which the vortices shed in the shear layer of the model.

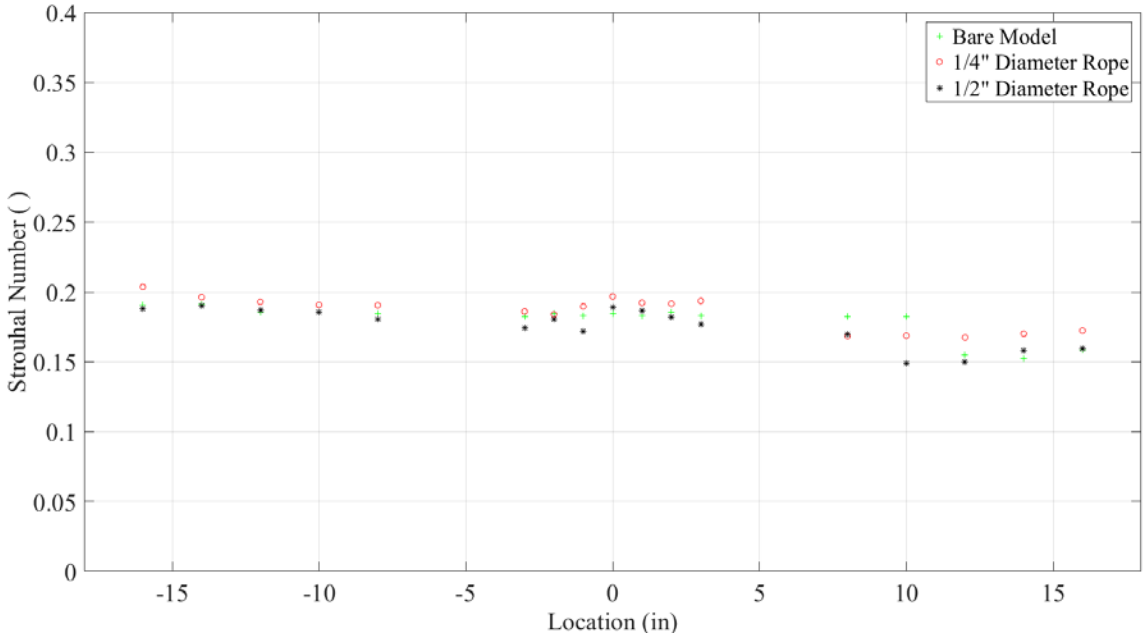

Figure 5.8 Strouhal numbers comparison of the 12-sided model in the face upwind configuration at Re = 44,000

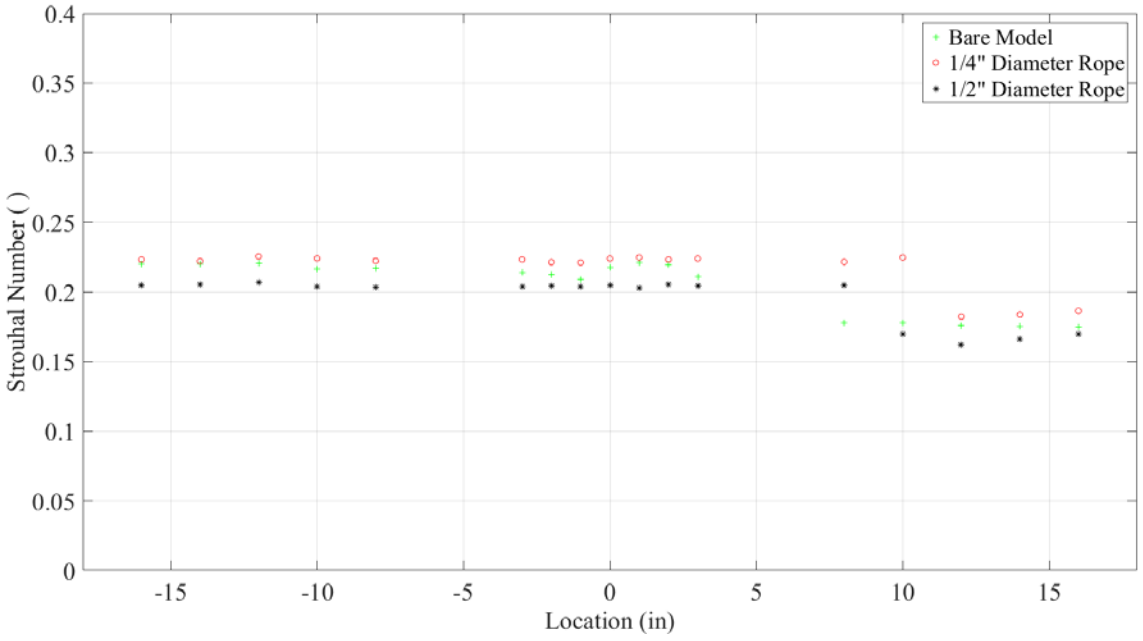

Figure 5.9 Strouhal numbers comparison of the 12-sided model in the vertex upwind configuration at Re = 44,000

5.3.3 16-Sided Model: Shedding Frequency Study

Figure 5.10 and Figure 5.11 present the resulting Strouhal values of the 16-sided model in both the face- and vertex-upwind positions. The figures relate any potential effects of the ¼ inch rope strake on the model.

Similar to the 12-sided model, it is difficult to clearly discern a pattern in the comportment of the bare versus straked model from the face upwind configuration on the 16-sided model, seen in Figure 5.10. Although disorganized, the model behaves in a locked-in mode with larger Strouhal values encountered at its thinner end.

From Figure 5.11, clearer and more constant Strouhal values are observed for the 16-sided model in the vertex upwind pattern than in the face upwind configuration. An almost constant value of 10 Hz is seen for two thirds of the model with a steep decrease near the thicker end of the model. The larger diameter area of the 16-sided model, being less slender and less flexible, is positively contributing to an overall decrease of the shedding frequency by approximately 2 Hz. Although the ¼ inch diameter rope is responsible for a fine downward shift of the frequency values, the model is still considered to be experiencing a lock-in occurrence across its span-wise direction.

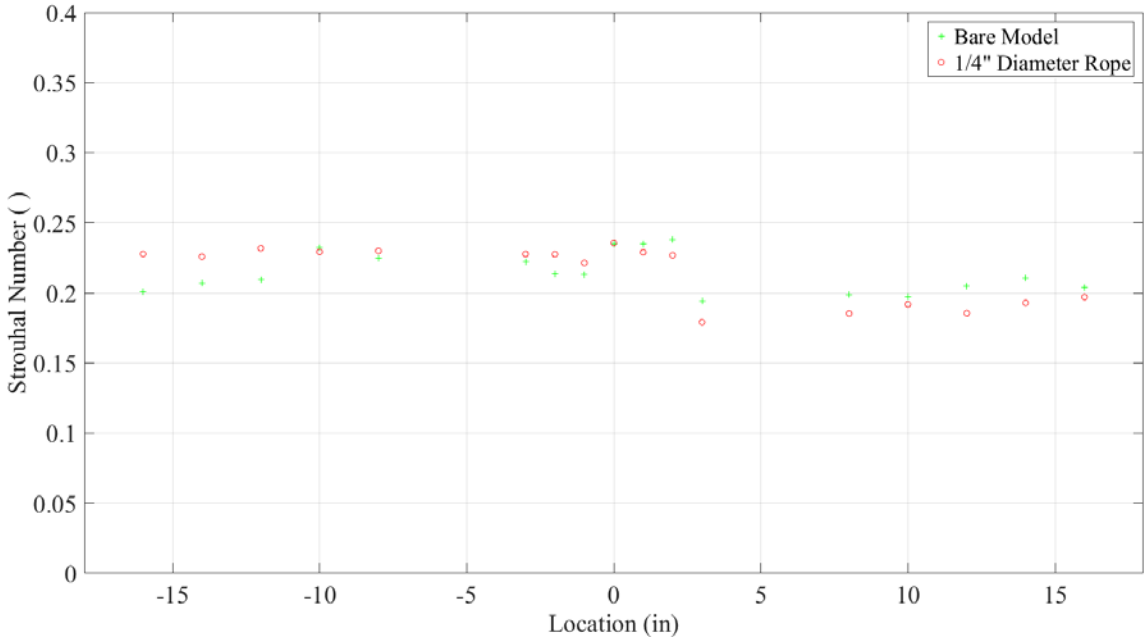

Figure 5.10 Strouhal numbers comparison of the 16-sided model in the face upwind configuration at Re = 44,000

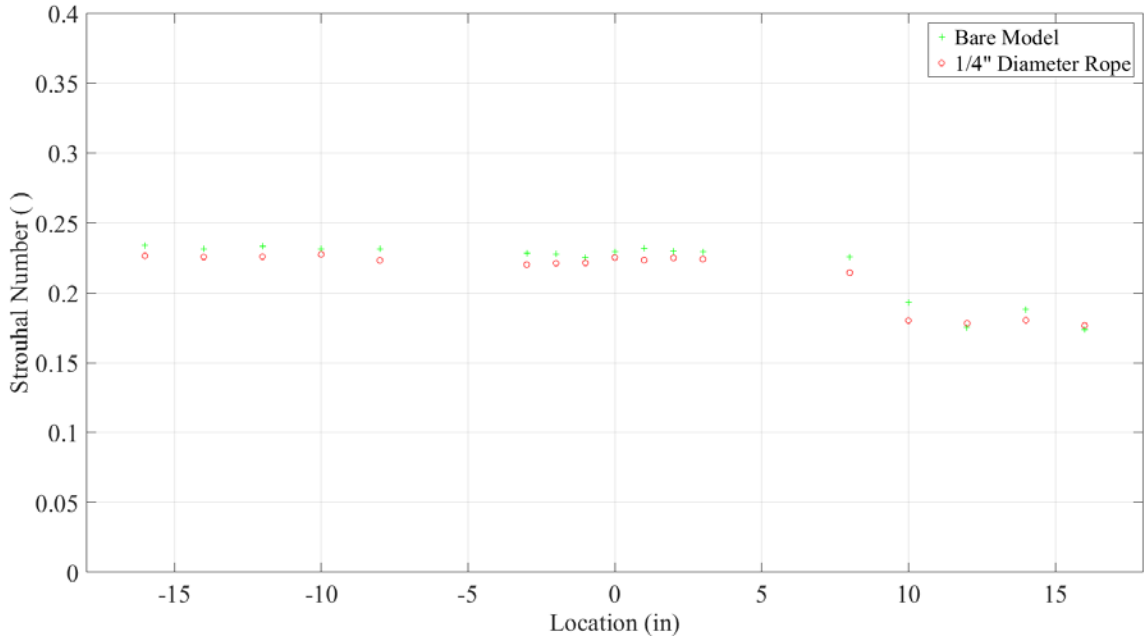

Figure 5.11 Strouhal numbers comparison of the 16-sided model in the vertex upwind configuration at Re = 44,000

5.4 Vortex Shedding Frequency Peaks

Due to a lack of definitive information gathered from the vortex shedding frequencies and Strouhal numbers results, a deeper investigation is necessary to acquire more information about the vibrational behavior of the HMLT models that are fitted with the helical strakes. The first step in determining if any performance changes occur on the retrofitted models is to directly compare the spectra from different cases.

Two examples have been chosen to examine the response of the HMLT model under different retrofit configurations.

Figure 5.12 shows the signal FFTs of the 12-sided model in the face upwind configuration at the span-wise center of the model. In addition to the bare model, the 0.05D and 0.1D (D being the diameter of the model) helical strake retrofits processed signals are transposed within the same graph. The bottom subplot is a zoomed in view of the top subplot to better perceive the vortex shedding frequency peak details. As observed previously in the shedding frequency plots, the ¼ inch diameter rope disruption shifts the frequency value to a larger amplitude. On the other hand, the ½ inch diameter has little effect on the location of the peak. Contrarily to the expected mitigated result, the shedding frequency response of the 12-sided model with either rope thicknesses is stronger. However, the width of the spectral peak appears to be wider for the model with the strakes. It can also be observed that the areas under the peak bandwidths are generally larger in size.

Figure 5.13 displays the signal FFTs of the 16-sided model in the vertex upwind configuration at the span-wise center of the model. The FFTs for both a bare model case and a ¼ inch diameter rope case are shown in the same graph. Similar to spectra from the

12-sided model, the figure is divided into two subplots with the bottom plot being a zoomed in version of the spectral peak. Note that the shedding frequency peak is stronger for the bare model with a height increment of approximately one third. Nonetheless, the ¼ inch diameter rope case exhibits a smoother behavior of the peak with a larger area and wider bandwidth.

In this case, it is important to investigate other aspects of the spectral peaks besides the vortex shedding frequencies. The observed differences from the stacked frequency spectrum plots suggests that some changes could have occurred after retrofitting the models, namely the strength of the peak and the area characteristics of the band surrounding the peaks. Consequently, the following traits of the spectra will be analyzed: signal strength, peak bandwidth area, and peak width. These aspects are discussed in the next three subsections of this chapter.

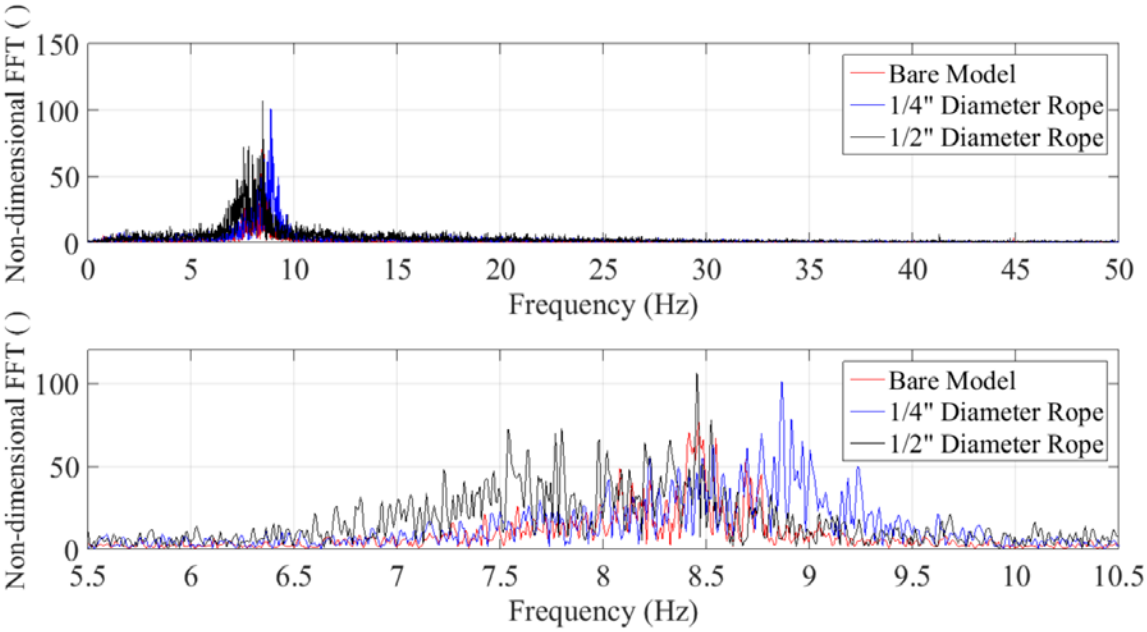

Figure 5.12 FFT comparison of the 12-sided model in the face upwind configuration for location “0” at Re = 44,000

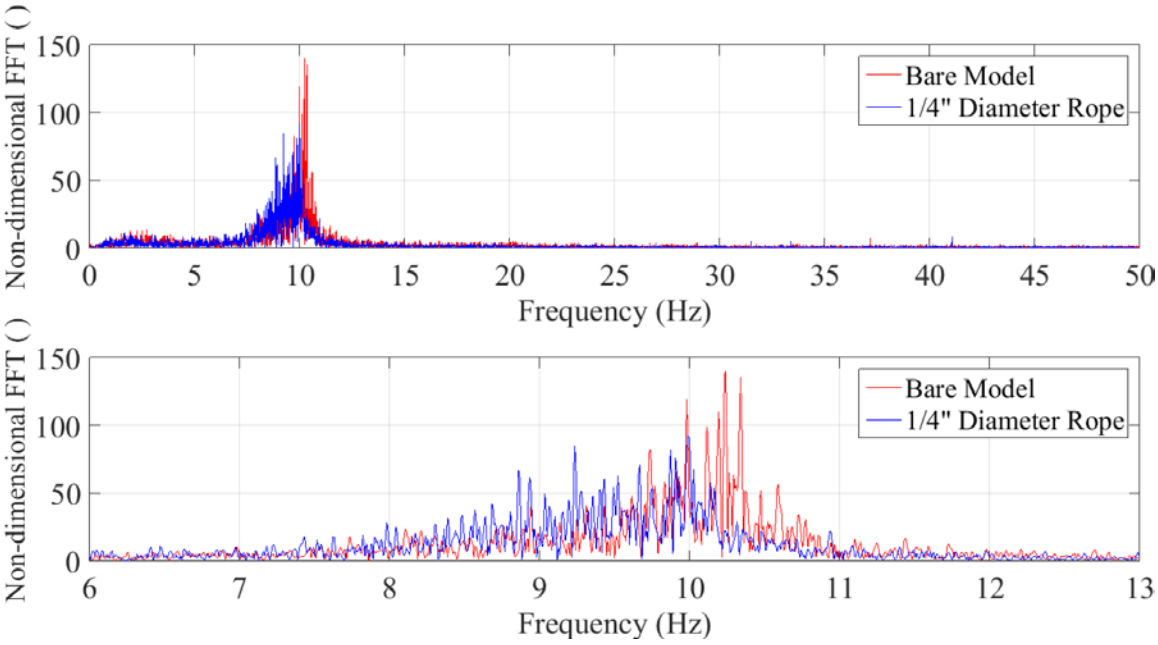

Figure 5.13 FFT comparison of the 16-sided model in vertex upwind configuration for location “0” at Re = 44,000

5.5 Peak Height Measurements: Signal Strength Study

The first feature of the vortex shedding peaks in the spectra that is examined is the strength of the signal or the height of said peak. It is important to note that the data was normalized prior to measuring the peak strength in order to standardize the attained results.

Figure 5.14 and Figure 5.15 compare the signal strengths of the 12-sided model response with and without a rope disruption for the face and vertex upwind configurations respectively. On the other hand, Figure 5.16 and Figure 5.17 summarize the strength of the 16-sided model vortex shedding frequency peaks, in a face and vertex upwind orientation respectively, with and without a helical strake retrofit.

From all the figures, one cannot clearly discern a pattern in the comportment of the bare versus straked model. The data within the peak height plots are disorganized with a combination of larger-strength, lower-strength, and similar strength amplitudes for either the bare models or the models fitted with helically patterned rope. Although no peculiarities in the conduct of any individual case are observed, the signal strengths tend to remain in the same general vicinity at the thicker end, middle, or thinner end of the models.

For all cases, the strongest peaks are observed near the center of the model. This effect is to be expected due the antenna-like nature of the hot-wire. The hot-wire is less likely to pick up noisy signals, as the location of the sensor is driven further away from the experiment's installation system and the wind tunnel's surrounding geometry.

The signal strength comparison of the 16-side model in the vertex upwind configuration, shown in Figure 5.17, is the only case that displays a lesser peak height at 13 out of 17 locations. The most noticeable reduction in the signal strength is towards the center of the model, likely due to a lack of interaction from the mounting setup.

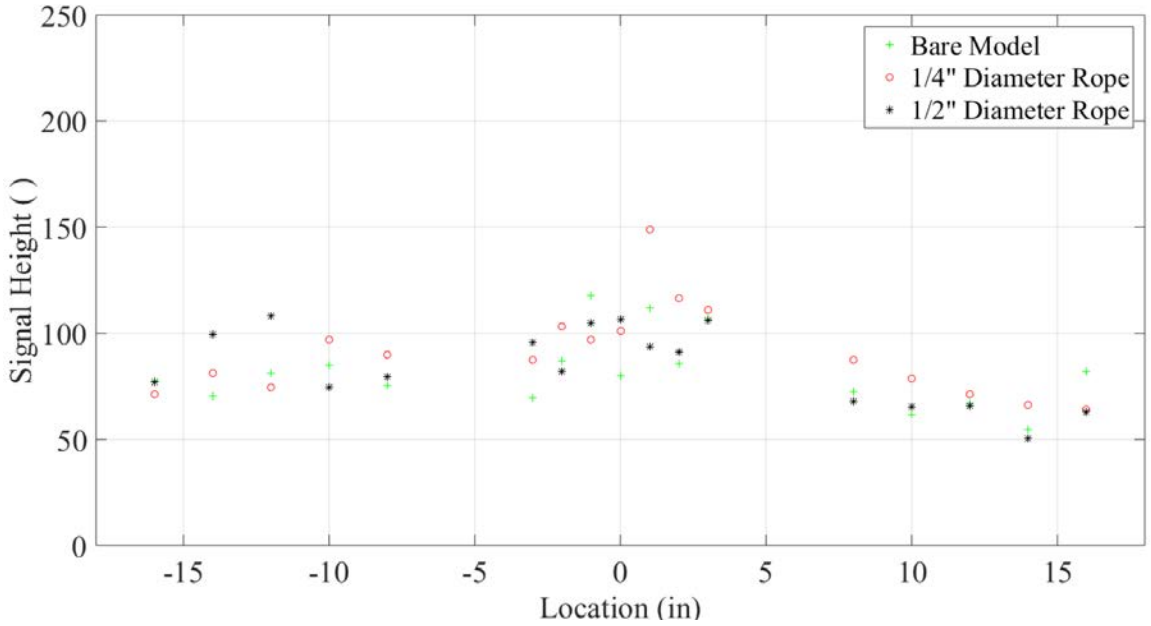

Figure 5.14 Signal strength comparison of the 12-sided model in the face upwind configuration at Re = 44,000

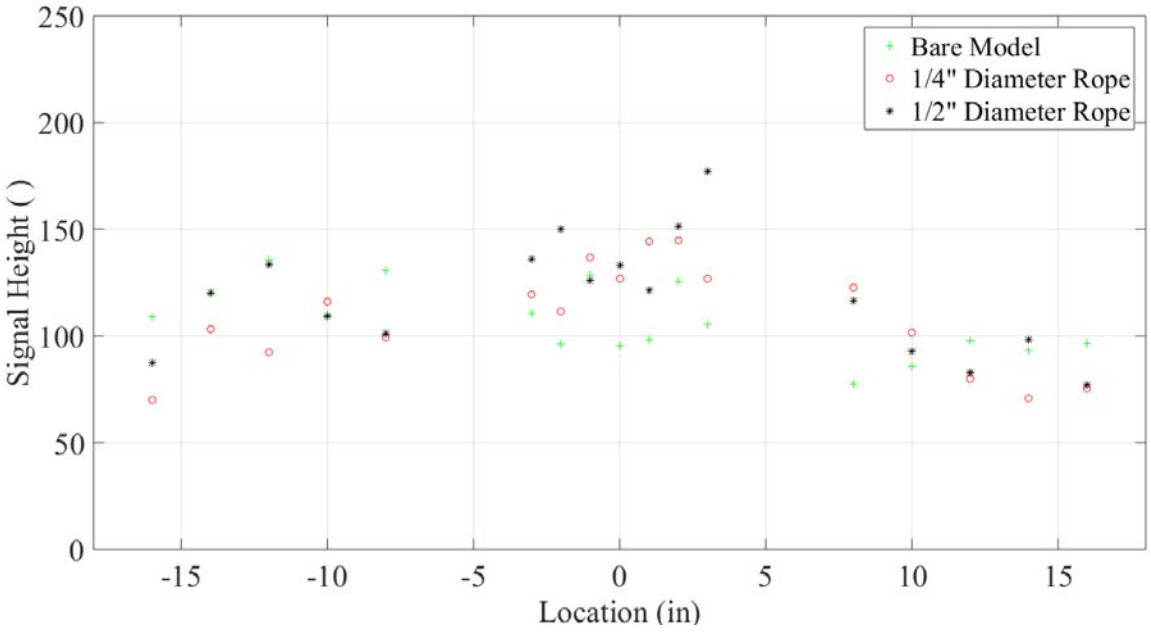

Figure 5.15 Signal strength comparison of the 12-sided model in the vertex upwind configuration at Re = 44,000

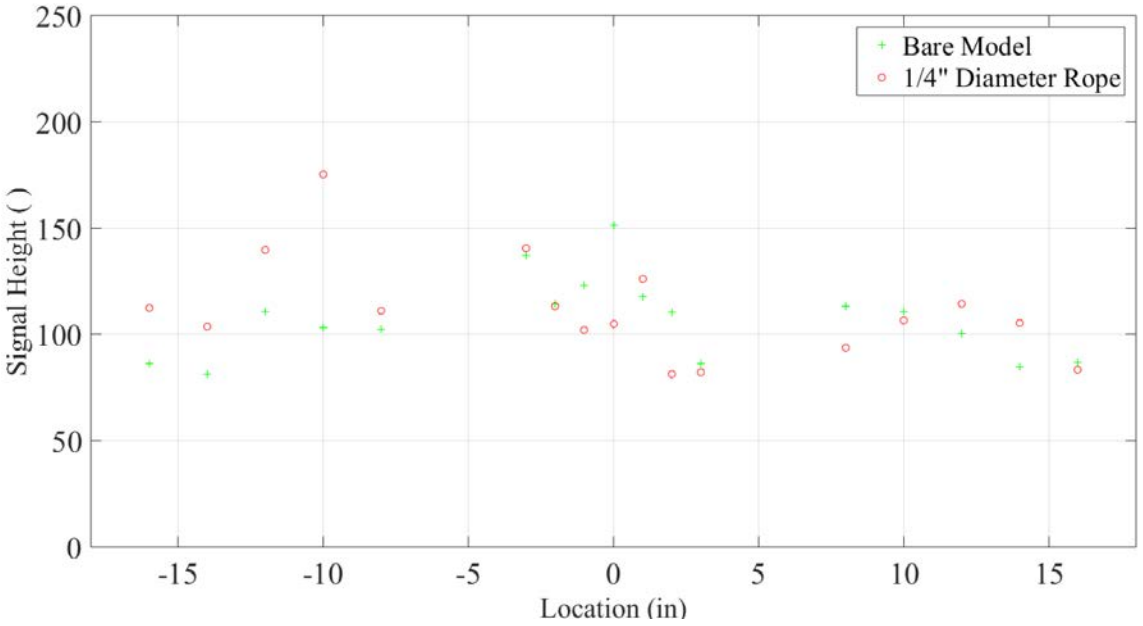

Figure 5.16 Signal strength comparison of the 16-sided model in the face upwind configuration at Re = 44,000

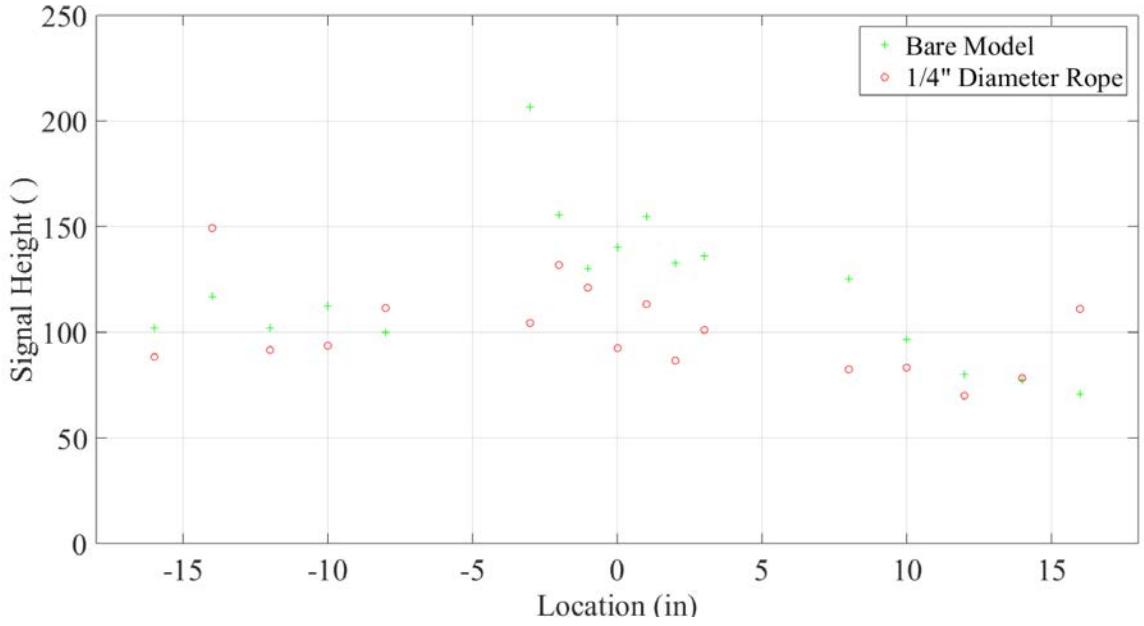

Figure 5.17 Signal strength comparison of the 16-sided model in the vertex upwind configuration at Re = 44,000

5.6 Peak Area Measurements

The second aspect of the spectra that is inspected is the area of the peak width. This vortex shedding frequency peak area is calculated by choosing a set distance, at an equivalent of 500 index points both left and right of the shedding frequency value, with the intention of normalizing the measured areas.

Figure 5.18 and Figure 5.19 present the signal peak areas of the 12-sided model response with and without a helical strake retrofit for the face and vertex upwind configurations respectively. While Figure 5.20 and Figure 5.21, correspondingly in a face and vertex upwind alignment, capture the peak area results of the 16-sided model in both a bare and helically patterned rope set up.

Looking at all the area plots, the most pronounced results are observed for 12-sided model in the face upwind configuration case. Figure 5.18 confirms the anticipated area increase for a model fitted with helical strakes. Two clear substantial upward shifts in the area values can be seen for the ¼ inch and ½ inch diameter rope cases. The FFT peak area increases as the thickness of the rope increases, suggesting that the signal might not be as strong for the model with the rope disruption. Furthermore, the area increase is indicative of a broader, more moderate, and less steep peak. This observation is considered to be a first sign that the helical strake ropes are favorably mitigating the effect of vortex induced vibrations and lock-in.

However, the vertex upwind configuration for the 12-sided model, seen Figure 5.19, does not completely agree with its face upwind counterpart. An area increase, with a corresponding rope thickness increase, is only observed near the thick end of the model, at locations 8 to 16 inches away from the center of the model. On the other hand, the

central range of the model is experiencing an adverse decrease of the area irrespective of the rope diameter. Lastly, the results at the thin end of the model do not show any clear patterns relating the thickness of the rope retrofit with the area.

The 16-sided model results for either direction configurations are indecisive. The face upwind case mostly presents a decrease in the spectral peak area when fitted with a ¼ inch rope, while the vertex upwind case shows very little differences between the peak areas of the bare model as opposed to the peak areas of the straked model.

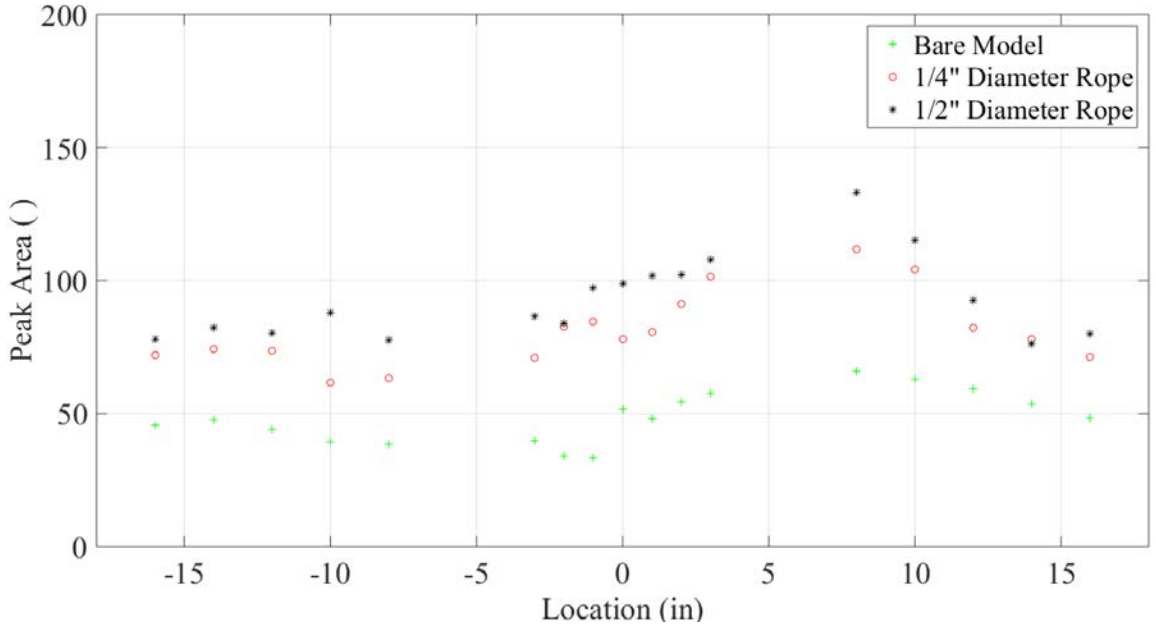

Figure 5.18 Area comparison of the 12-sided model in the face upwind configuration at Re = 44,000

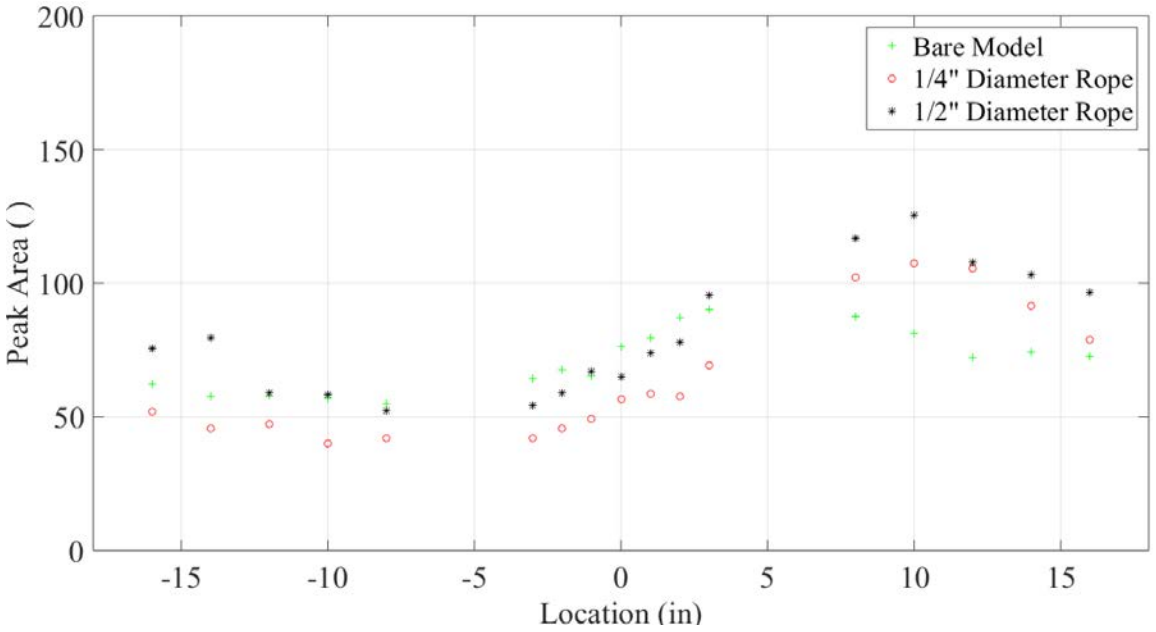

Figure 5.19 Area comparison of the 12-sided model in the vertex upwind configuration at Re = 44,000

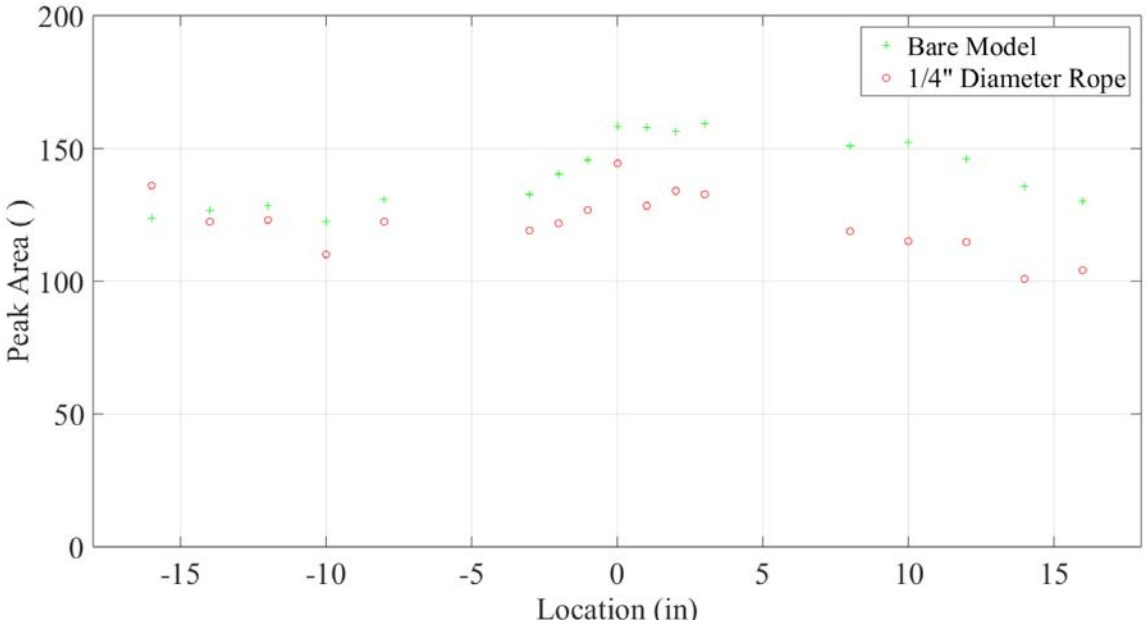

Figure 5.20 Area comparison of the 16-sided model in the face upwind configuration at Re = 44,000

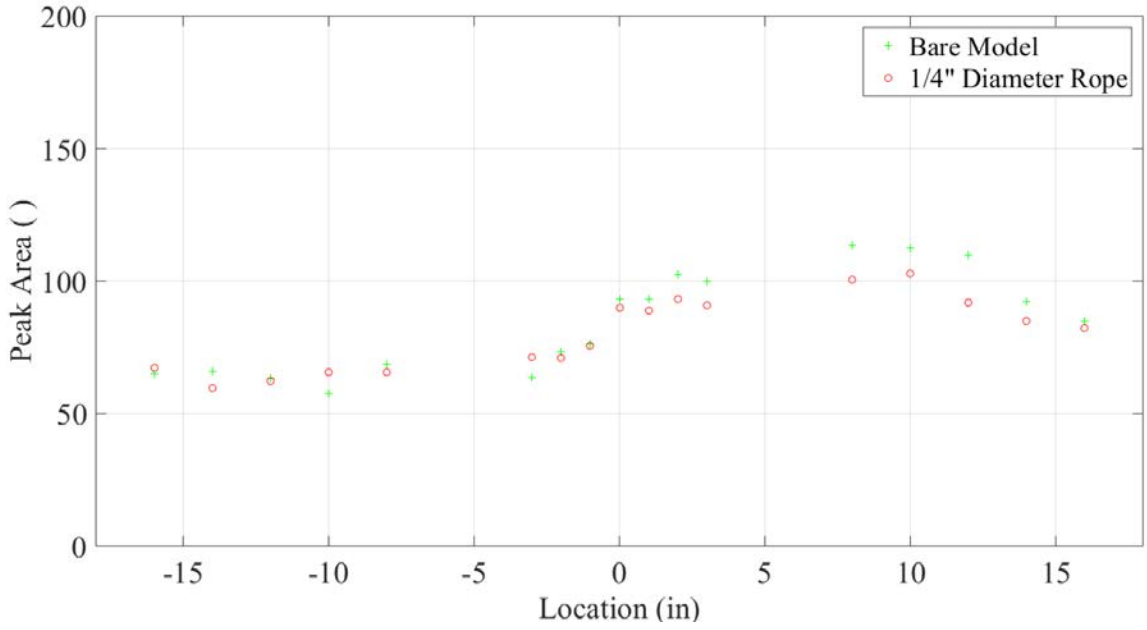

Figure 5.21 Area comparison of the 16-sided model in the vertex upwind configuration at Re = 44,000

5.7 Peak Width Measurements

In a last attempt at finding a quantifiable spectral change to document any definite behavior changes, the width of the spectral peak is measured. The width is calculated by dividing the area under the peak by the signal height. An exhaustive summary of the results for all the studied cases can be seen in Figures Figure 5.22 thru Figure 5.25. Figure 5.22 and Figure 5.23 present the width measurements of the 12-sided model under the face and vertex upwind configurations, while Figure 5.24 and Figure 5.25 display the peak widths for the 16-sided model.

In retrospect to the peak area measurements for the 12-sided model in the face upwind orientation, the peak width results present a similar behavior with a global increase in value corresponding with an increase in the rope thickness. The growth in the peak widths suggests a wider and smoother signal confirming the results found from the area data.

The 12-sided vertex upwind case, shown in Figure 5.23, disagrees with the face upwind case with no clear pattern in the span-wise direction of the model. While the thicker end of the model demonstrates an increase in the peak width, although unrelated to the thickness of the rope, the central area of the model shows a decrease in the peak width with the addition of the rope disruption. Conversely, the thin end of the model depicts little change in relation to the rope.

Other configurations such as the 16-sided model do not show any correlation between the bare model and the installation of the rope. Both the face and vertex upwind cases portray a combination of decreased, increased, and similar width measurements regardless of the span-wise location on the model. The differences of the peak width values for the vertex

upwind case are less prominent than for the face upwind case. This could be attributed to the already lower values for the vertex upwind configuration where an earlier transition to separation occurs due to the model's sharp edge that is directly facing the flow direction.

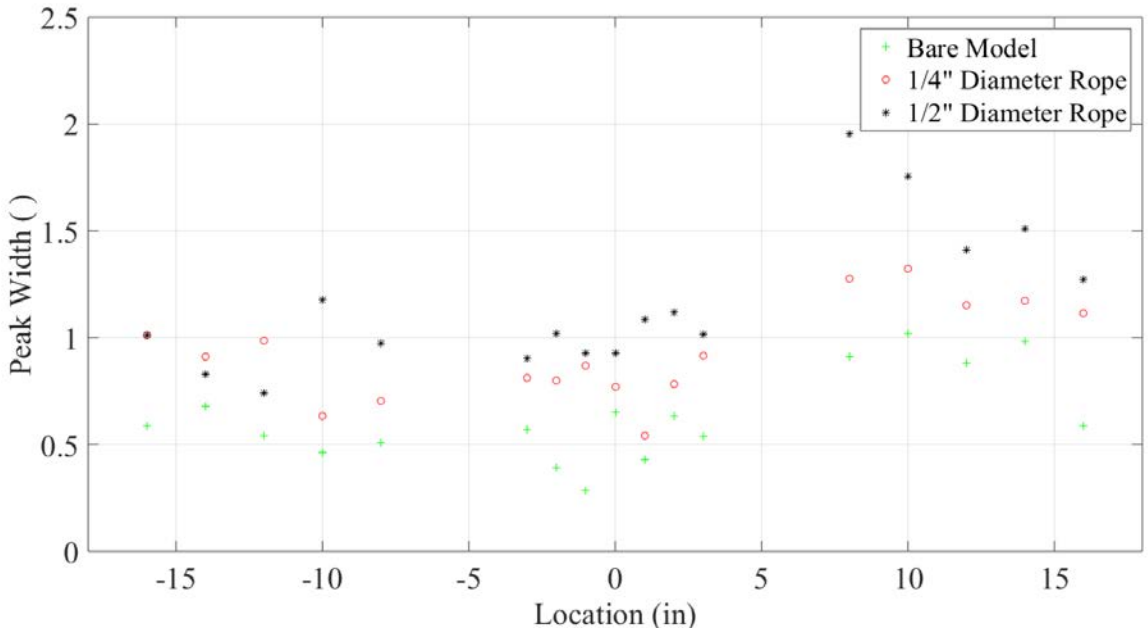

Figure 5.22 Peak width comparison of the 12-sided model in the face upwind configuration at Re = 44,000

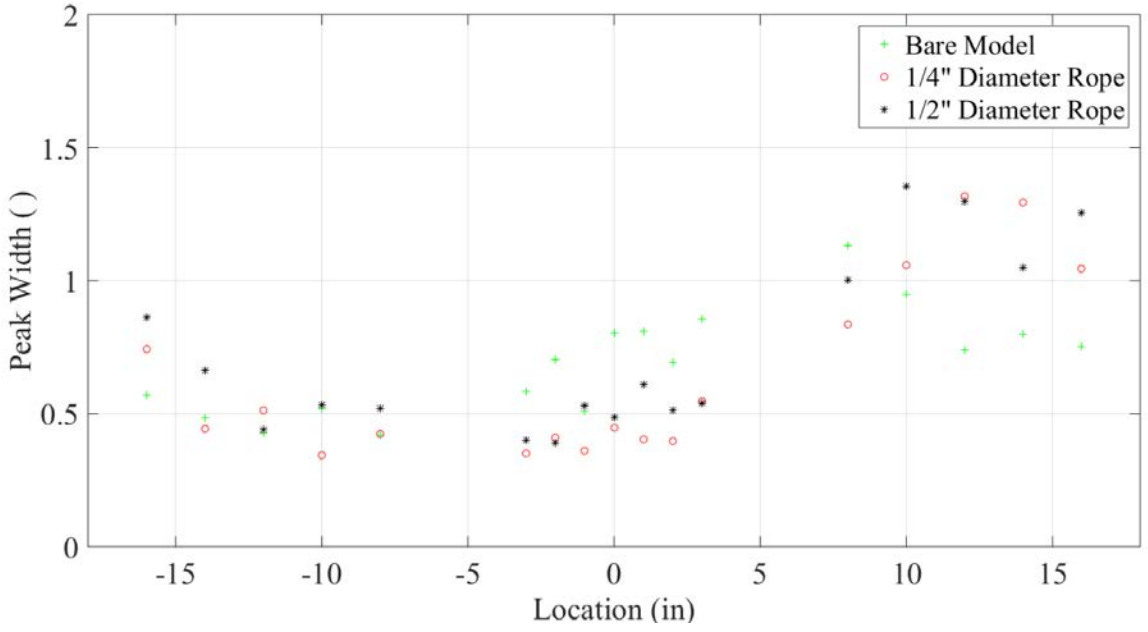

Figure 5.23 Peak width comparison of the 12-sided model in the vertex upwind configuration at Re = 44,000

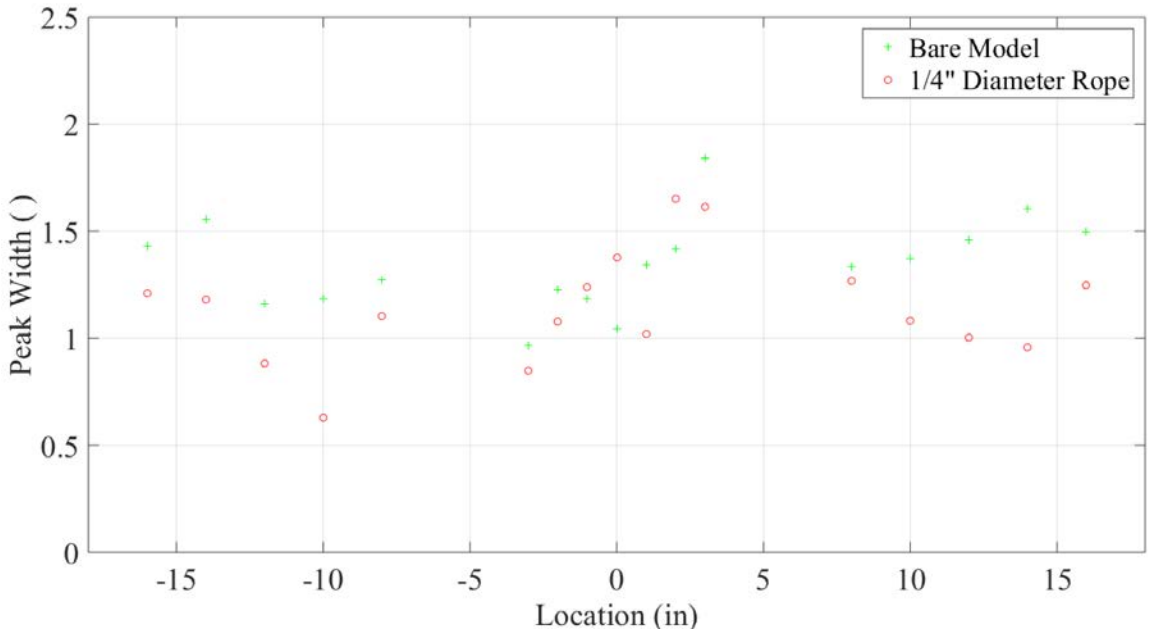

Figure 5.24 Peak width comparison of the 16-sided model in the face upwind configuration at Re = 44,000

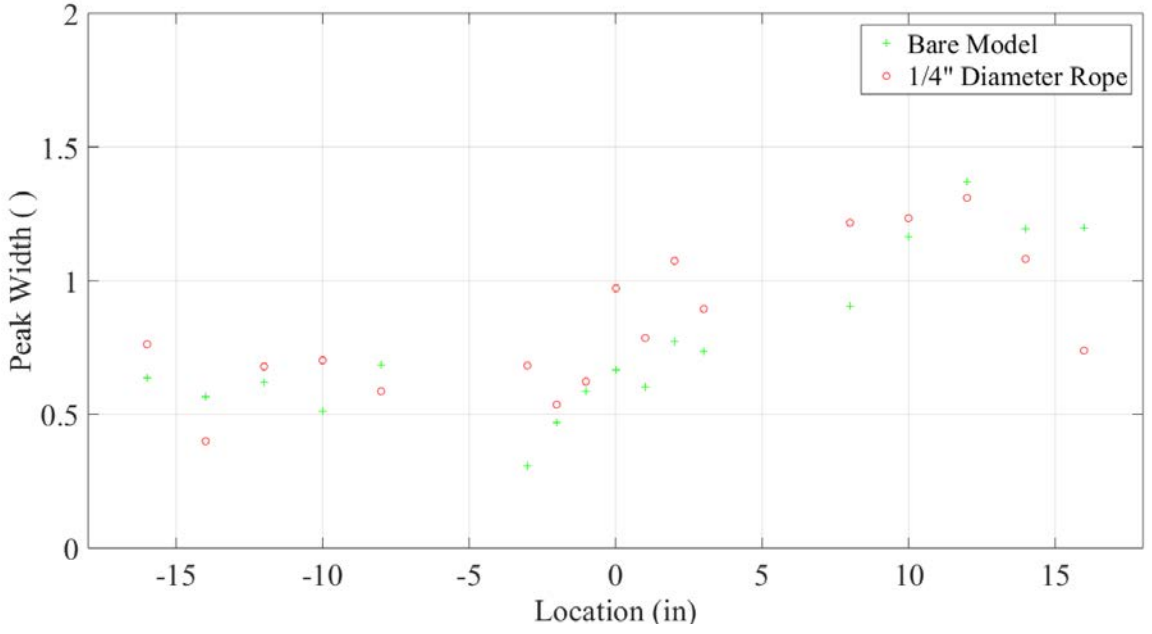

Figure 5.25 Peak width comparison of the 16-sided model in the vertex upwind configuration at Re = 44,000

CHAPTER 6. CONCLUSIONS AND RECOMMENDATIONS

6.1 Conclusions

This thesis presents an experimental research study that was performed on high mast lighting towers retrofitted with helical strakes. The study was conducted in a subsonic wind tunnel setting on two scaled models that were equipped with different diameter ropes. The purpose of this project was to analyze the effects of helical strakes on the vortex induced vibrations experienced by high mast lighting towers and the resulting lock-in. The lock-in phenomenon is characterized by a near constant shedding frequency value regardless of the diameter changes within the tapered high mast lighting towers. Extensive research studies, both in the computational and experimental disciplines, have been carried out to implement mitigation methods in order to control vortex induced vibrations. Different mechanisms have been successful in curbing vortex induced vibrations and the resulting lock-in phenomenon in both civil and marine applications. However, most research pertaining to mitigation devices has been restricted to cylinders only.

In the study pertaining herein, different aspects of the collected data was studied including vortex shedding frequencies, Strouhal values, signal strengths, signal areas, and signal widths within the spectra of velocity fluctuations in the wake. The results confirmed some positive responses for the 12-sided model in the face upwind

configuration in mitigating vortex induced vibrations. However, not all cases showed improvements in the behavior of the models and some cases even presented adverse effects on the response of the model from the addition of the helical strakes.

In conclusion, no one measure has proven to be clearly decisive for both models in all cases. Some clear patterns can be seen for the 12-sided model in the face upwind configuration when looking at the area and width of the vortex shedding frequency peaks, but the other cases show no distinct behavioral changes.

Although inconclusive, the results give good insight on the methods that are used to study the performance of helical strakes in mitigating the oscillations attributed to vortex shedding and the lock-in phenomenon. The lack of influence of the rope streamlining method could be attributed to various reasons, including but not limited to the size of the scaled model, the size of the ropes and their pitch distance, the wind tunnel effects, or even the instrumentation. Any one of these reasons could have clouded the frequency signal responses of the models and/or altered the behavior of the HMLTs in a controlled setting.

6.2 Recommendations

Further investigation is required to extensively understand the vortex induced oscillation behavior of HMLTs when retrofitted with helical strakes. Although the possibilities for other studies are endless, the following suggestions can be exploited in a different project:

- Alter the strake pitch diameter;
- Alter the rope diameter;
- Partially cover the model with strakes;
- Use of a damper;
- Apply surface perturbations;
- Apply other suppression devices including but not limited to fairings, fins, shroud sleeves, and slats.

LIST OF REFERENCES

LIST OF REFERENCES

[1] R. J. Connor, National Research Council (U.S.). Transportation Research Board., National Cooperative Highway Research Program., American Association of State Highway and Transportation Officials., and United States. Federal Highway Administration., *Fatigue loading and design methodology for high-mast lighting towers* (NCHRP report,, no. 718). Washington, D.C.: Transportation Research Board, 2012, pp. 72, A-29, B-30 p.

[2] J. A. Ocampo, "Vortex shedding lock-in on tapered bodies of various polygonal cross-sections," Ph.D., Purdue University, 2013.

[3] E. B. Ahearn and J. A. Puckett, "Reduction of Wind-Induced Vibration in High-Mast Light Poles," University of Wyoming, LaramieFHWA-WY-10/02F, 2010.

[4] B. M. Phares, P. P. Sarkar, W. T. J., and B. chang, "Development of fatigue procedure for slender, tapered support structures for highway signs, luminaires, and traffic signals subjected to wind-induced excitation from vortex-shedding and buffeting," Iowa State University,2007.

[5] L. Caracoglia and N. P. Jones, "Numerical and experimental study of vibration mitigation for highway light poles," *Engineering Structures,* vol. 29, no. 5, pp. 821 - 831, 2007.

[6] M. P. Repetto and G. Solari, "Wind-induced fatigue collapse of real slender structures," *Engineering Structures,* vol. 32, no. 12, pp. 3888-3898, 12// 2010.

[7] J. Anderson, M.-H. Education, Ed. *Fundamentals of Aerodynamics*, 5th Edition ed. 2010.

[8] B. N. Pamadi, *Performance, Stability, Dynamics, and Control of Airplanes*, 2nd ed. (AIAA Education Series). AIAA, 2004, p. 780.

[9] E. L. Houghton, P. W. Carpenter, S. H. Collicott, and D. T. Valentine, *Aerodynamics for Engineering Students*, 6th ed. Elsevier, 2012.

[10] M. Van Dyke, *An Album of Fluid Motion*, 4th Edition ed. Stanford, California: The Parabolic Press, 1988, p. 176.

[11] J. H. Lienhard, "Bulletin 300 Synopsis of lift, drag, and vortex frequency data for rigid circular cylinders" ed. Pullman, Washington: Technical Extension Service, 1966, p. 32.

[12] I. Giosan and P. Eng, "Vortex Shedding Induced Loads on Free Standing Structures," in "Structural Vortex shedding Response Estimation Methodology and Finite Element Simulation,"

[13] R. A. Kumar, C.-H. Sohn, and B. H. L. Gowda "Passive control of vortex-induced vibrations: An overview," *Recent Patents on Mechanical Engineering,* vol. 1, no. 1, pp. 1-11, 2008.

[14] O. H. Ammann, T. Von Karman, and G. B. Woodruff, *The failure of the Tacoma Narrows bridge; a report to the Honorable John M. Carmody, Administrator, Federal Works Agency, Washington, D.C.* Pasadena,: Board of Engineers, 1941.

[15] J. K. Vandiver, "Damping Parameters for flow-induced vibration," *Journal of Fluids and Structures,* vol. 35, pp. 105 - 119, 2012.

[16] Y. Tamura, K. Fujii, T. Ohtsuki, T. Wakahara, and R. Kohsaka, "Effectiveness of tuned liquid dampers under wind excitation," *Engineering Structures,* vol. 17, no. 9, pp. 609 - 621, 1995.

[17] M. M. Zdravkovich, "Review and classification of various aerodynamic and hydrodynamic means for suppressing vortex shedding," *Journal of Wind Engineering and Industrial Aerodynamics,* vol. 7, no. 2, pp. 145 - 189, 1981.

[18] P. W. Bearman, J. Owen, and A. A. Szewczyk, "Vortex shedding and drag force reduction," 2005. Available: https://www.google.ch/patents/US6908063.

[19] T. Zhou, S. F. Razali, Z. Hao, and L. Cheng, "On the study of vortex-induced vibration of a cylinder with helical strakes," *Journal of Fluids and Structures,* vol. 27, no. 7, pp. 903 - 917, 2011.

[20] G. S. Baarholm, C. M. Larsen, and H. Lie, "Reduction of VIV using suppression devices—An empirical approach," *Marine Structures,* vol. 18, no. 7–8, pp. 489 - 510, 2005.

[21] S. Huang, "VIV suppression of a two-degree-of-freedom circular cylinder and drag reduction of a fixed circular cylinder by the use of helical grooves," *Journal of Fluids and Structures,* vol. 27, no. 7, pp. 1124 - 1133, 2011.

[22] C.-K. Chyu and D. Rockwell, "Near-Wake Flow Structure of a Cylinder with a Helical Surface Perturbation," *Journal of Fluids and Structures,* vol. 16, no. 2, pp. 263 - 269, 2002.

APPENDICES

Appendix A Reynolds Number Sample Calculation

The Reynolds number used during the study is computed by using the following definition: $Re = \frac{U_\infty D}{\nu} = \frac{U_\infty D \rho}{\mu}$

First, the air density is computed using the Ideal Gas Law $P = \rho RT$ from the ambient pressure *P*, the ambient temperature *T*, and the specific gas constant *R*.

Given the ambient pressure P = $100x10^3$ Pa, temperature T = 30 ºC = 303.15 K, and the ideal gas constant R = 287.058 J kg^{-1} K^{-1}, the air density can be calculated as:

$\rho = P/RT = 1.1491$ kg/m^3.

Next, the free stream velocity U_∞ is computed using Bernoulli's equation: $U_\infty = \sqrt{\frac{2\Delta P}{\rho}}$.

The total and static pressure difference, ΔP, is collected from the panel connected to the wind tunnel. In the specific example in this appendix, the pressure difference reading is 0.074 in.H2O = 18.4389 Pa. Using Bernoulli's equation, the free stream velocity is U_∞ = 5.6649 m/s.

Finally, using the model diameter of 5 inches and a dynamic viscosity value of μ = $1.8608x10^{-5}$ kg/ms (from Sutherland's Law), the Reynolds number is computed to Re = 44,430.

Appendix B MATLAB Code Files

The following code is used to extract the collected data from the hot-wire using the oscilloscope.

```
%%%%%%%%%%%%%%%%%%%%%%%%%%%%%%%%%%%%%%%%%%%%%%%%%%%%%%%%%%%%%%%%%%%%%%%%%%%%%%%%
% Read_Data.m
% Extract and Save Data
% Ayah Zahour
% Fall 2016
%%%%%%%%%%%%%%%%%%%%%%%%%%%%%%%%%%%%%%%%%%%%%%%%%%%%%%%%%%%%%%%%%%%%%%%%%%%%%%%%
%% Clear any previous information
clc
clear

%% Extract data from the saved data files

% Use "csvread" function to import the raw data: "30" being the first
% row offset, "100029" being the last row offset,"0" being the first
% and only column offset
data = csvread('SONI3872.csv',30,0,[30 0 100029 0]);

%% Save the data
save data
```

The following code is used to filter and process the previously extracted data to yield the final results.

```
%%%%%%%%%%%%%%%%%%%%%%%%%%%%%%%%%%%%%%%%%%%%%%%%%%%%%%%%%%%%%%%%%%%%%%%%%%%%
% Process_Data.m
% Process Data and Print Results
% Ayah Zahour
% Fall 2016
%%%%%%%%%%%%%%%%%%%%%%%%%%%%%%%%%%%%%%%%%%%%%%%%%%%%%%%%%%%%%%%%%%%%%%%%%%%%
%% Define the variables
Fs = 1e3;                       % Sampling frequency
T = 1/Fs;                       % Sample time
L = 100000;                     % Length of signal
pf = 5;                         % Padding Factor
L2 = pf*L;                      % Signal length for zero padding

%%%%%%%%%%%%%%%%%%%%%%%%%%%%%%%%%%%%%%%%%%%%%%%%%%%%%%%%%%%%%%%%%%%%%%%%%%%%
%% Filter the signal

% Subtract Mean Voltage
data_1_1 = data - mean(data);

% Cosine Window
w = 0.5*(1-cos(2*pi*(0:(L-1))/(L-1)))';
Wout = w.*data_1_1(:,1);

% Zero Padding
Wout(L+1:L2) = 0;

% Convolve
c = conv([Wout], [1,1]/2);

%% Create FFT and cut any data above 50Hz

% FFT
NFFT = 2^nextpow2(L);
Y = fft(c,NFFT)/L;
f = Fs/2*linspace(0,1,NFFT/2+1);
YY =2*abs(Y(1:NFFT/2+1));

% Normalize the data
norm = 1/sum(YY.^2);
YY = YY*norm;

% Cut Data after 50Hz to discard of the 60 Hz peak
icut = 50;                      % Define a frequency value to cut
f(f>icut) = 0;                  % Replace all Frequencies > icut with 0
f(1) = 1;                       % Set the first index to 1, not to be
                                  removed by the subsequent line
f(f==0) = [];                   % Remove all trailing zeros with an empty
                                  array
```

```
f(1) = 0;                    % Restore the value of the first index
                               back to 0
y1 = YY(1:length(f));
[y_max, index] = max(y1)     % Find the y-location of the max peak and
                               its index
F_shed = f(index)            % Find the shedding frequency value

%%%%%%%%%%%%%%%%%%%%%%%%%%%%%%%%%%%%%%%%%%%%%%%%%%%%%%%%%%%%%%%%%%%%%%%%%%%%
%% Define a band around the peak using index values

% Find the indices of the start and end of the peak bandwidth
x_a_peak_start_index = index - 500;
x_a_peak_end_index = index + 500;

% Find the start and end 'x' location of the FFT peak bandwidth
x_a_peak_start = f(x_a_peak_start_index);
x_a_peak_end = f(x_a_peak_end_index);

%%%%%%%%%%%%%%%%%%%%%%%%%%%%%%%%%%%%%%%%%%%%%%%%%%%%%%%%%%%%%%%%%%%%%%%%%%%%
%% Find area under the curve up to the end of the peak bandwidth

% Subtract Mean Voltage
data_1_1 = data - mean(data);

% Cosine Window
w = 0.5*(1-cos(2*pi*(0:(L-1))/(L-1)))';
Wout_1 = w.*data_1_1(:,1);

% Zero Padding
Wout_1(L+1:L2) = 0;

% Convolve
c_1 = conv ([Wout_1], [1,1]/2);

% FFT
NFFT_1 = 2^nextpow2(L);
Y_1 = fft(c_1,NFFT_1)/L;
f_1 = Fs/2*linspace(0,1,NFFT_1/2+1);
YY_1 =2*abs(Y_1(1:NFFT_1/2+1));

% Normalize the data
norm_1 = 1/sum(YY_1.^2);
YY_1 = YY_1*norm_1;

% Cut Data after end of bandwidth
icut_1 = x_a_peak_end;       % Define a frequency value to cut
f_1(f_1>icut_1) = 0;         % Replace all Frequencies > icut with 0
f_1(1) = 1;                  % Set the first index to 1, not to be
                               removed by the subsequent line
f_1(f_1==0) = [];            % Remove all trailing zeros with an empty
                               array
f_1(1) = 0;                  % Restore the value of the first index
                               back to 0
```

```
y1_1 = YY_1(1:length(f_1));

%Find the area under the curve up to the end of the bandwidth
A_1 = trapz (f_1, y1_1);

%%%%%%%%%%%%%%%%%%%%%%%%%%%%%%%%%%%%%%%%%%%%%%%%%%%%%%%%%%%%%%%%%%%%%%%%%%%%%%%
%% Find area under the curve up to the start of the peak bandwidth

% Subtract Mean Voltage
data_1_2 = data - mean(data);

% Cosine Window
w = 0.5*(1-cos(2*pi*(0:(L-1))/(L-1)))';
Wout_2 = w.*data_1_2(:,1);

% Zero Padding
Wout_2(L+1:L2) = 0;

% Convolve
c_2 = conv ([Wout_2], [1,1]/2);

% FFT
NFFT_2 = 2^nextpow2(L);
Y_2 = fft(c_2,NFFT_1)/L;
f_2 = Fs/2*linspace(0,1,NFFT_2/2+1);
YY_2 =2*abs(Y_1(1:NFFT_2/2+1));

% Normalize the data
norm_2 = 1/sum(YY_2.^2);
YY_2 = YY_2*norm_2;

% Cut Data after start of bandwidth
icut_2 = x_a_peak_start;     % Define a frequency value to cut
f_2(f_2>icut_2) = 0;         % Replace all Frequencies > icut with 0
f_2(1) = 1;                  % Set the first index to 1, not to be
                               removed by the subsequent line
f_2(f_2==0) = [];            % Remove all trailing zeros with an empty
                               array
f_2(1) = 0;                  % Restore the value of the first index
                               back to 0
y1_2 = YY_2(1:length(f_2));

% Find the area under the curve up to the start of the bandwidth
A_2 = trapz (f_2, y1_2);

%%%%%%%%%%%%%%%%%%%%%%%%%%%%%%%%%%%%%%%%%%%%%%%%%%%%%%%%%%%%%%%%%%%%%%%%%%%%%%%
%% Compute the area under the peak band curve and peak width
% Find and print the area between start and end of the peak bandwidth
A = A_1 - A_2

% Find and print the "Rectangle" width of the peak from the area of the
bandwidth
W = A/y_max
```